

Dust semi-direct effects: The influence of free-tropospheric dust-induced longwave radiation on low-level cloud response over the North Atlantic Ocean

Satyendra K. Pandey and Adeyemi A. Adebiyi

5

Department of Life and Environmental Sciences, University of California - Merced, Merced, CA, USA

Correspondence to: Satyendra K. Pandey (spandey9@ucmerced.edu)

Adeyemi A. Adebiyi (aaadebiyi@ucmerced.edu)

10 Abstract

Aerosol semi-direct effect is the adjustment of the radiative budget due to the cloud response to radiation absorption. Although dust accounts for about a third of aerosols' shortwave absorption, our understanding of its semi-direct effect often relies on traditional shortwave-focused mechanisms previously established for biomass-burning aerosols, and implications of dust longwave absorption on clouds have yet to be explored. Here, we assess the low-level cloud cover (LLCC) response to changes in properties and characteristics of the free-tropospheric dust layer over the North Atlantic Ocean (May-August, 2007-2017). We find that, consistent with previous studies, LLCC typically responds positively (increases in clouds) to an overlying dust layer. However, this response weakens with increasing dust optical depth (DOD), dust geometric thickness (DGT), and dust-layer base height (DBH). Specifically, we find that the LLCC response weakens by $4.3 \pm 1.04\%$ and $1.6 \pm 0.65\%$, respectively, for a one-standard-deviation increase in DOD and DGT, and a smaller response to DBH ($0.19 \pm 0.45\%$). We also find that the weakened LLCC response is primarily due to enhanced dust-induced longwave-dominated cloud-top warming, which counteracts the mean cloud-top cooling by as much as 19% (mean of 9%). Sensitivity analysis further indicates that the variability in dust properties, influenced by dust size distribution and refractive index, dominates the changes in dust-induced cloud-top warming, rather than variabilities in cloud properties or thermodynamic profiles. Our result adds to the traditional understanding of LLCC enhancement through shortwave-driven atmospheric stability, often associated with aerosol semi-direct effects, and highlights the role of dust-induced cloud-top longwave warming in dust semi-direct effects.

Keywords: Dust; Longwave semi-direct effect; Cloud-top radiative cooling; Low-level clouds

30 1 Introduction

Atmospheric aerosols remain a complex but important component of the Earth's climate system, representing a major source of uncertainties in our understanding of the current climate and its future projections (Bellouin, 2015; Bellouin et al., 2020; Bender, 2020; Forster et al., 2023). This is because aerosols can interact with the climate system through several complex pathways, influencing the overall

35 radiative budget at the surface and top of atmosphere (Bellouin et al., 2020; Li et al., 2022; Satheesh and Krishnamoorthy, 2005). For example, aerosols can directly impact the climate by scattering and absorbing solar and terrestrial radiation (Atwater, 1970; Chlek and Coakley, 1974). It can also impact climate indirectly by serving as cloud condensation nuclei or ice nuclei, influencing cloud formation, reflectivity, and lifetime (Albrecht, 1989; Twomey, 1974). Another way aerosols influence climate without
40 contributing to cloud formation is by modulating the thermodynamic profiles of atmosphere where clouds exist (Allen et al., 2019; Amiri-Farahani et al., 2017; Baró Pérez et al., 2021; Hansen et al., 1997; Herbert et al., 2020; Johnson et al., 2004; Koren et al., 2004; Lu et al., 2021). This latter pathway of aerosol-climate interactions, called aerosol semi-direct effect (SDE), is the adjustment of the radiative budget at the top of the atmosphere due to the cloud response to aerosol radiation absorption (Hansen et al., 1997;
45 Johnson et al., 2004; Koren et al., 2004). Previous studies have suggested that aerosol semi-direct effects could warm or cool the climate system, depending on the relative vertical position of the aerosol and cloud layers (Koch and Del Genio, 2010). However, our understanding of the exact processes that establish this aerosol semi-direct effect remains very limited, contributing a substantial fraction to the uncertainties associated with aerosol-radiation interactions and, consequently, the overall radiative budget
50 at the top of the atmosphere (Adebiyi et al., 2023; Bellouin et al., 2020; Forster et al., 2023; Koch and Del Genio, 2010). Further, it remains unclear whether these processes related to aerosol semi-direct effects are consistent across the different absorbing aerosols in the atmosphere, including biomass-burning and mineral dust aerosols, and to what degree they may differ.

55 Most previous studies estimating aerosol semi-direct effects have largely focused on biomass-burning smoke aerosols, including black carbon, that dominate absorbing aerosols in the atmosphere, and these studies have shaped our general understanding of processes associated with SDE (Bond et al., 2013; Jacobson, 2014; Koch and Del Genio, 2010; Mallet et al., 2020). Specifically, these studies have indicated that the semi-direct effects of biomass-burning aerosols and the corresponding cloud response depend on cloud type, aerosol properties, and the relative position of the aerosol and cloud layers (Haywood et al.,
60 2020; Herbert and Stier, 2023; Wilcox, 2010). For example, when biomass-burning aerosols are within a cloud layer, the warming due to shortwave absorption can '*burn off*' the cloud, decreasing the cloud cover, which produces a positive semi-direct effect (Johnson et al., 2004; Koren et al., 2004). On the other hand, when the biomass-burning aerosols are distinctly above the cloud layer, the shortwave warming can increase the lower tropospheric stability, increasing the moisture build-up in the boundary layer and
65 resulting in increased cloud cover and a negative semi-direct effect (Wilcox, 2012). Although semi-direct effects from biomass-burning aerosols occur for all cloud types, their influences are by far the most substantial on marine low-level clouds (Koch and Del Genio, 2010), dominating the aerosol-cloud processes and, therefore, the overall aerosol radiative effects over the Southeast Atlantic Ocean (Zuidema et al., 2016). Globally, low-level clouds are widespread and constitute about 40 % of all overall cloud
70 occurrences (Schneider et al., 2013; Stubenrauch et al., 2013), with single-layer low-level clouds, such as

stratocumulus clouds, covering about one-fifth of the global ocean (Hahn and Warren, 2007). Given the widespread presence of marine low-level clouds co-existing with other absorbing aerosols, our understanding of the aerosol semi-direct effect that relies on processes associated with biomass-burning smoke aerosols alone is, therefore, incomplete.

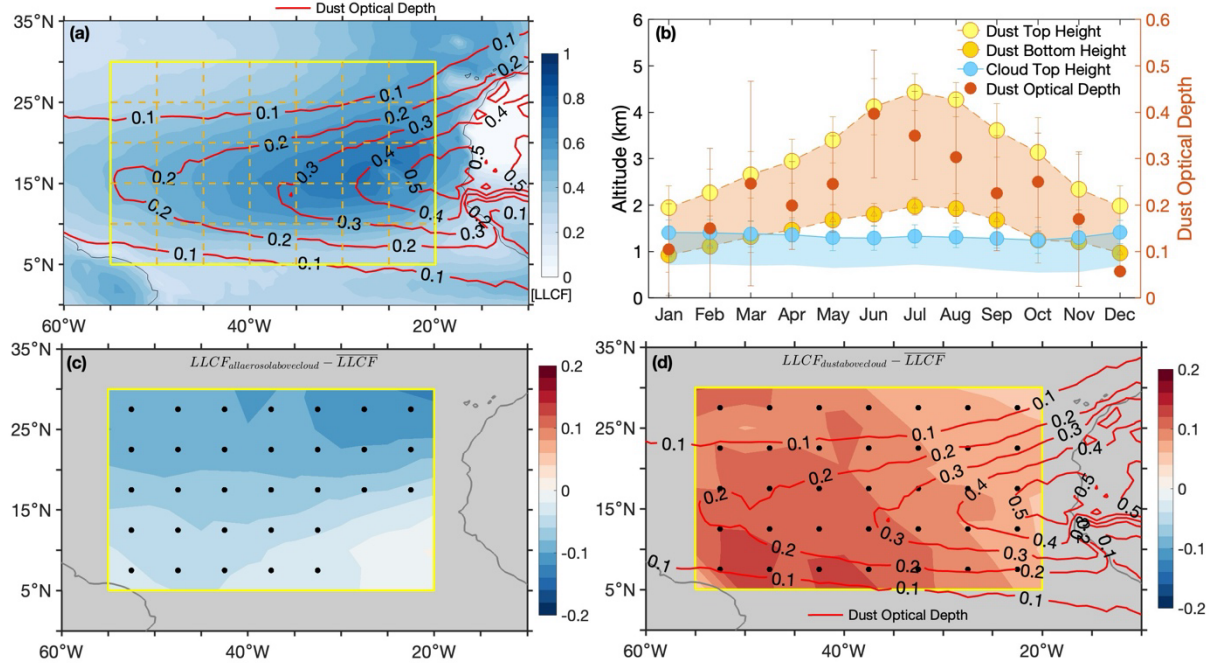


Figure 1: (a) The spatial distribution of low-level cloud fraction (shaded contour) and column dust optical depth (red line contours). The yellow box represents the analysis domain, which consists of $5^\circ \times 5^\circ$ grid boxes used for categorization in our analysis (see Section 2.2). **(b)** The annual cycle of dust and cloud layer top and base height averaged over the analysis domain (yellow box in (a)). **(c)** & **(d)** Changes in low-level cloud fraction relative to a long-time mean over the region when (c) all aerosols and (d) only dust are present above the cloud layer. Black dots show locations that are significant at the 95 % confidence level with a two-tailed Student t-test. The cloud fraction was taken from MODIS Aqua and dust optical depth from CALIPSO Level 2 datasets between May and August 2007 and 2017.

Although most studies shaping our understanding of aerosol semi-direct effects focus on biomass-burning smoke aerosols, few studies have examined semi-direct effects for mineral dust aerosols – another major absorbing aerosol that accounts for about 30% of the shortwave absorption in the atmosphere (Sand et al., 2021). Moreover, mineral dust also accounts for about two-thirds of all aerosol mass in the atmosphere, with more than 50 % emitted from the North African Deserts and transported westward over the North Atlantic Ocean in what is called the Sahara Air Layer (SAL) (Adebiyi et al., 2025; Kok et al., 2021a; Prospero et al., 2021). Over the ocean, these North African dust aerosols interact with one of the major

low-level cloud regions (Fig. 1a), influencing the radiative budget at the top of the atmosphere (Wood, 2012). During the spring and summer, the SAL has an average separation from the underlying low-level clouds of about 0.12 km that maximizes in July (Fig. 1b). In contrast, during the winter, the dust layer is 95 generally transported at a lower altitude, allowing the dust particles to mix with the low-level clouds. Previous studies have suggested that dust SDE and the associated low-level cloud responses are similar to those described by biomass-burning aerosols (Amiri-Farahani et al., 2017; DeFlorio et al., 2014; Doherty and Evan, 2014; Huang et al., 2006). That is, when dust aerosols are within the low-level cloud 100 layer, dust SDE is positive with a decrease in low-level cloud cover, while when dust is above the cloud layer, dust SDE is negative with an increase in cloud cover. Over the North Atlantic Ocean, the enhancement in low-level cloud cover is generally positive during the summer when the dust is above the cloud (about +8% increase for the domain shown in Fig. 1d) compared to when other aerosols are above 105 the cloud (-6% decrease for the same domain region shown in Fig. 1c). In addition, similarly to studies of biomass-burning aerosols, these previous studies have linked the enhancement of low-level cloudiness and the associated negative dust SDE to the above-cloud dust layer to stronger lower-tropospheric inversion caused by dust-induced shortwave heating near the cloud top (DeFlorio et al., 2014; Doherty and Evan, 2014).

However, unlike biomass-burning aerosols, atmospheric dust contains a significant fraction of coarser 110 particles (diameter $\geq 2.5 \mu\text{m}$) that can interact with longwave radiation and, therefore, impact dust semi-direct effect differently from other absorbing aerosols (Adebiyi et al., 2023; Adebiyi and Kok, 2020; Kok et al., 2017, 2021b). Specifically, previous studies leveraging in-situ dust measurements have shown that 115 dust particles larger than $5 \mu\text{m}$ are about four times more abundant in the atmosphere than previously estimated by climate models (Adebiyi and Kok, 2020). Furthermore, observations also showed that these coarse dust aerosols can have sizes up to about $60 \mu\text{m}$ in the atmosphere, making them an important component that cannot be ignored in estimating dust radiative impacts (Adebiyi et al., 2023; Ryder et al., 2013, 2018, 2019; Weinzierl et al., 2017). Because coarse-mode dust absorbs and scatters more longwave 120 radiation than fine-mode dust, it can significantly cool the dust layer in the longwave, counteracting the warming effect of shortwave radiation and, therefore, may influence the overall dust semi-direct effect and associated low-level cloud response (Kok et al., 2023). In addition, dust-induced longwave radiation can be emitted towards the low-level clouds, potentially impacting the cloud-top processes that deviate from the traditional process of SDE by biomass-burning aerosols.

Furthermore, this potential dust-induced longwave influence on dust's semi-direct effect and its low-level 125 cloud response could depend on the properties and characteristics of the dust layer. One parameter that can influence the dust-induced longwave absorption within the dust layer and the associated downwelling radiation is the dust extinction or optical depth, which, in turn, depends on the dust size distribution and dust complex refractive index (Gkikas et al., 2022; Zheng et al., 2023). For example, the vertical

distribution of coarse dust within the dust layer can affect the vertical distribution of dust absorption, the dust-layer longwave cooling, and the magnitude of downwelling radiation, thereby influencing potential interactions with underlying low-level clouds. In addition, for the same optical properties, the altitude and 130 geometric thickness of dust layer can also influence the amount of radiation reaching the cloud top. These inferences were recently made for biomass-burning smoke aerosols by Herbert et al. (2020), who used large eddy simulation to show the sensitivity of the cloud properties and the resulting semi-direct effect to the variability in the altitude and layer characteristics of the smoke overlying the low-level cloud over the Southeast Atlantic Ocean. While this assessment was conducted using model simulation and only for 135 biomass-burning aerosols, it remains unclear exactly how observed variabilities in optical properties and dust-layer characteristics, including the dust layer altitude, its geometric thickness, and separating distance, will affect the underlying low-level cloud, its response to radiative warming or cooling, and ultimately the dust semi-direct effect.

To fill this gap, this study seeks to understand how the above-cloud Sahara air layer influences the dust 140 semi-direct effect over the North Atlantic Ocean by examining the impacts of dust optical depth and dust-layer characteristics on underlying low-level cloud response using satellite observations. Specifically, we leveraged aerosol and cloud information from CALIOP (Cloud-Aerosol Lidar with Orthogonal Polarization) onboard CALIPSO (Cloud-Aerosol Lidar and Infrared Pathfinder Satellite Observation) satellite and cloud profiling radar (CPR) aboard CloudSat. We hypothesize that the influence of above- 145 cloud dust on low-level cloudiness varies depending on the characteristics of the dust layer, specifically the dust-base altitude and geometric thickness. Whereas the dust-base height (DBH) characterizes the proximity of the dust and cloud layers, the dust geometrical thickness (DGT) represents the vertical extent of the dust layer. Our results show a reduction in mean cloud cover with an increase in dust geometrical thickness, regardless of dust-base heights, whereas cloud response to dust-base height depends on the 150 thickness of the layer. Additionally, with constant base altitude and geometrical thickness, our results also show a negative cloud cover sensitivity with increasing dust optical depth that depends on the dust size distribution and the complex refractive index of the dust layer. We find that these responses in cloud cover to changes in dust-layer properties and characteristics primarily occur through dust modulation of the longwave fluxes reaching the cloud top, which reduces the mean cloud-top cooling.

2 Data and Methods

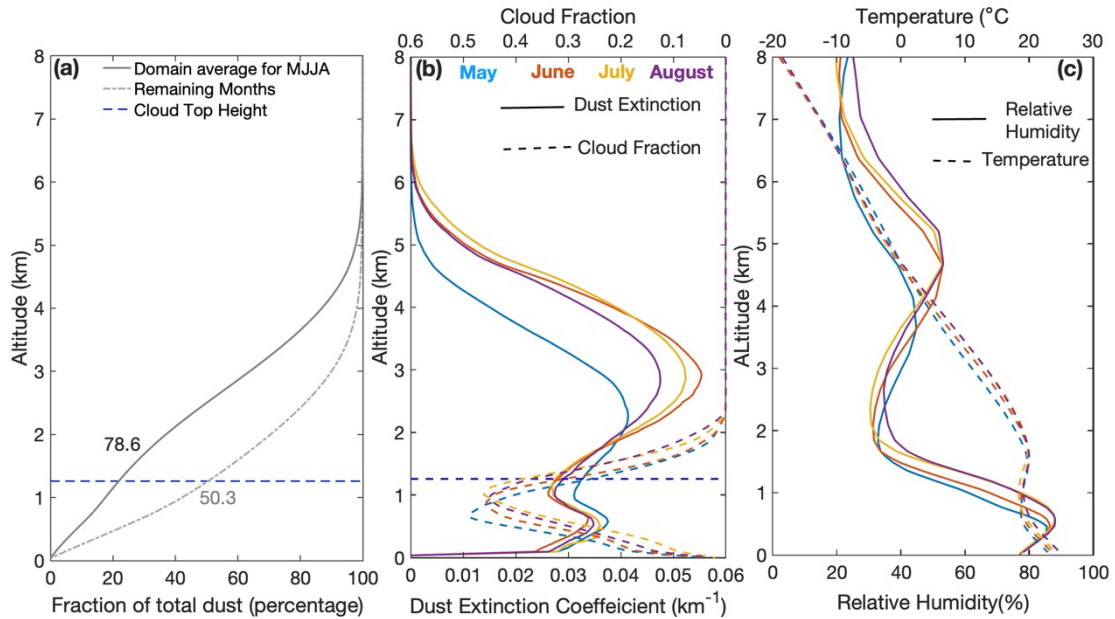


Figure 2: (a) The domain mean profiles depict the fraction of dust concentration (in percentage) that lies below a particular altitude relative to the total column burden. Each point on the line represents the percentage of dust occurring below a specific altitude relative to the total column burden. The solid line represents the domain average profile for May to August, while the dashed line indicates the average values for the remaining months. The horizontal blue line denotes the mean low-level cloud top, and the numerical annotations beside each line indicate the dust percentage above the cloud top. **(b)** The domain-mean monthly profile of the dust extinction coefficient (solid lines) and low-level cloud fraction (dashed lines; note that the values go from right to left at the top of the figure). **(c)** The domain-mean monthly profiles of relative humidity (solid lines) and temperature (dashed lines). Colors in (b) & (c) indicate months with blue for May, red for June, orange for July, and purple for August. The datasets span from 2007 to 2017, with temperature and humidity profiles obtained from auxiliary meteorological data provided as part of CALIOP level 2 data products.

We focused our analysis on the North Atlantic Ocean between May and August (2007-2017) when the SAL dust frequently overlies low-level cloud layers (Fig. 1b). Specifically, during this period, there is a higher probability of dust being present above the clouds than during other periods of the year, allowing for enough data samples for statistically significant analysis (e.g., see supplementary Fig S1). When averaged over the domain of interest (see Fig. 1a), approximately 79% of the total column dust burdens are located above the mean low-level cloud top between May and August (Fig. 2a), compared to only about 50% during other months. Compared to the May-August period, most of the above-cloud dust

occurrences in other months are in March and April, with relatively lower overall dust optical depth (see 180 red dots in Fig. 1b) and higher probability of mid-to-high level cloud occurrences that can influence our analysis. Furthermore, the domain mean dust extinction profiles peak between May and August, with the column-integrated optical depth maximizing in June (≈ 0.4 ; Fig. 2b and Fig. 1b). To this end, our analysis also examines the possible confounding influence of aerosol optical depth on the cloud response to dust-layer characteristics during the period.

185 2.1 Datasets

We obtained aerosol, cloud, and radiative flux information from satellite-based observations, and meteorological parameters, including temperature and humidity, from reanalysis datasets. The satellite-based observations include those from CALIOP (Cloud-Aerosol Lidar with Orthogonal Polarization) 190 onboard the CALIPSO (Cloud-Aerosol Lidar and Infrared Pathfinder Satellite Observation) satellite, cloud profiling radar (CPR) aboard CloudSat, and reanalysis data from the European Centre for Medium-Range Weather Forecasts (ECMWF).

2.1.1 Aerosols and Cloud Data

We relied on CALIOP for vertically resolved measurements of cloud and aerosol (Winker et al., 2010). Equipped with an onboard lidar, this remote sensing platform measures the backscatter signal of clouds 195 and aerosols at two wavelengths, 532 nm and 1024 nm, and with distinct vertical resolutions: 30 meters from the surface to 8.2 km, 60 m from ≈ 8.2 km to ≈ 20.2 km, and 180 m above ≈ 20.2 km. Cloud and aerosol features are identified using the contrast between backscatter signals from the target feature and the altitude-based threshold defined for the clear air (Vaughan et al., 2009). The backscattered signal at 200 532 nm is preferred due to its sensitivity to a wider range of atmospheric targets, including small aerosol particles (Liu et al., 2004; Vaughan et al., 2009). The altitude boundaries of the identified features (aerosols or clouds) are determined iteratively using an algorithm known as the Selective Iterated Boundary Location Algorithm (SIBYL) (Hunt et al., 2009; Vaughan et al., 2002, 2009). The retrieved altitudes of the top and bottom boundaries of both cloud and aerosol layers have been extensively 205 validated under different atmospheric conditions at various locations (Candlish et al., 2013; Lu et al., 2021a; Mamouri et al., 2009; Perrone et al., 2011). Compared to ground-based lidar measurements, aerosol and cloud layer top boundaries are generally found within the range of 100 m (Kim et al., 2008; Lu et al., 2021b). However, several studies (Jethva et al., 2014; Rajapakshe et al., 2017) have observed that CALIOP underestimated the altitude of the bottom boundary of the aerosol layer compared to ground-based observations in earlier versions of the product. The latest release has improved this issue (Lu et al., 210 2021).

We use the latest version 4 (V4), level 2 (L2) merged layer products of CALIOP, which have a 5-km horizontal resolution, to determine the dust geometric thickness and the vertical position of dust and cloud layers (Liu et al., 2019). This version of CALIOP features an improved discrimination algorithm that can 215 more effectively differentiate between aerosol and cloud compared to the previous version (Liu et al., 2009). In addition, the enhanced algorithm also has improved classification capabilities, particularly in detecting lofted dust and smoke layers (Liu et al., 2019), which were occasionally misclassified as cirrus clouds in previous versions (Chen et al., 2010). Similarly, aerosol type discrimination has also undergone 220 significant modification, using input variables such as location, surface type, estimated particulate depolarization ratio, and integrated attenuated backscatter to identify specific aerosol types (Kim et al., 2018a; Omar et al., 2009). Overall, the identified aerosol types in V4 products are marine, polluted continental/smoke, clean continental, polluted dust, elevated smoke, dusty marine, and pure dust (Kim et al., 2018). Among these aerosol types, the identification of dust types (polluted dust, dusty marine, and pure dust) mainly depends on the estimated particle depolarization ratio, which quantifies the degree to 225 which the light scattered by atmospheric particles undergoes depolarization. Specifically, polarization refers to the orientation of the electric field vector of light waves, which can be altered upon scattering by particles. This ratio is linked to particle shape; spherical particles (such as marine aerosols or spherical droplets) have smaller effects on the polarization of incident light, resulting in low depolarization ratios, while non-spherical particles like mineral dust modulate the polarization more strongly, leading to higher 230 ratios. In V4 products, layers with a high particulate depolarization ratio estimated to be greater than 0.20 are classified as pure dust, regardless of surface type, location, altitude, or integrated attenuated backscatter values, owing to predominantly non-spherical particles. Conversely, moderately depolarizing particles, with a depolarization ratio ranging from 0.075 to 0.20 and a layer base height below 2.5 km when observed over the ocean, fall into the category of dusty marine particles. When these identical, 235 moderately depolarizing particles are detected above land or have a layer base height exceeding 2.5 km over ocean surfaces, they are labeled as polluted dust. Also, low depolarizing particles with a depolarization ratio of less than 0.075 are classified as polluted dust when found above desert surfaces and have a 532 nm integrated attenuated backscatter value greater than 0.0005. Because we focus on the SAL dust layer above the marine low-level clouds (generally above 2.5 km, see section 2.1.2 below), we 240 used only aerosol layers identified as “pure dust” in this study. We consider only pure dust to avoid any contamination of sea salt aerosols in dusty marine aerosol types, which can be substantial, especially close to the ocean surface, and have a depolarization ratio like those used for dusty marine (Sakai et al., 2010).

We estimated the geometrical thickness and separation distance of the identified dust layer from the low- 245 level cloud top using the ‘Layer Top Altitude’ and ‘Layer Base Altitude’ information provided in the L2 Merged Layer product (CAL_LID_L2_05km). Specifically, we estimated geometric thickness as the difference between the layer top and base altitudes of the dust layer, and similarly, we estimated the separating distance as the difference between the dust-layer base altitude and the cloud-layer top altitude.

Additionally, we obtained the dust optical depth as the aerosol optical depth (AOD) at 532 nm for 250 identified pure-dust-only profiles, with no other aerosol layers found above or below it at the same location. Although our estimated dust optical depth likely underestimates the column dust optical depth over the location since it considers only the pure dust layer, this underestimation has little to no impact on this study's conclusion since our analysis focuses on the sensitivity of low-level clouds to a unit change in dust properties. For both aerosols and cloud parameters, we used only daytime retrievals for our 255 analysis. We do so for two reasons: the first reason is that the daytime and nighttime retrievals for merged CALIPSO-CloudSat products are limited only between 2006 and 2011 because CloudSat switched to daytime-only operation after October 2011 due to a battery malfunction (Nayak et al., 2012; Witkowski et al., 2018). Because our analysis is between 2007 and 2017, which extends past the October 2011 260 timeline of daytime-only products, we use only daytime datasets to maintain consistency across the observation period. The second reason is that our analysis focuses on understanding both the shortwave and longwave influences of dust-layer characteristics on clouds, in contrast to similar analyses of smoke aerosols (e.g., Herbert et al., 2020). Since nighttime analysis only provides the effect of longwave radiation, we use daytime data to assess the influence of both shortwave and longwave radiation by SAL dust on low-level clouds.

265 2.1.2 Radiative Flux Data

In addition to aerosol information from CALIPSO, we also obtained radiative fluxes and heating rates from merged CALIPSO-CloudSat datasets that leverage instruments on the CALIPSO and CloudSat satellites. To estimate shortwave and longwave radiative effects, we used radiative fluxes and associated 270 heating rates from the 2B-FLXHR-LIDAR product (Henderson et al., 2013; L'Ecuyer et al., 2008), which includes measurements from the CPR aboard CloudSat, cloud and aerosol information from CALIOP, and other required variables from passive sensor MODIS aboard the Aqua satellite. For example, these 275 radiative flux products used cloud parameters, including information on cloud ice and liquid water content, as well as effective radii, derived from CloudSat retrievals and the aerosol profile information obtained from CALIPSO. In addition, the radiative fluxes also use aerosol optical properties (such as asymmetry parameter and single-scattering albedo) obtained from D'Almeida et al. (1991), and surface properties, such as surface albedo and emissivity, are sourced from the International Geosphere-Biosphere Program (IGBP). Furthermore, atmospheric parameters (surface pressure, surface temperature, as well as 280 profiles of pressure, temperature, specific humidity, and ozone mixing ratio) used for the radiative flux calculation were obtained from the European Centre for Medium-Range Weather Forecasts (ECMWF) reanalysis dataset and provided in the CloudSat dataset as ECMWF-AUX product (Cronk, 2017). The meteorological profiles and surface parameters from ECMWF 3-hour fields, given at a $0.5^\circ \times 0.5^\circ$ horizontal resolution, are interpolated to match the CPR geolocation, vertical bin, and time (Cronk, 2017). These aerosol and cloud parameters and the meteorological information are provided in a radiative

transfer model called BugsRad (Fu and Liou, 1992) to obtain radiative fluxes at a vertical resolution of 285 240 m. The uncertainties of the obtained fluxes were assessed by performing multiple sensitivity analyses and comparing them with the top-of-atmosphere fluxes obtained from the Clouds and the Earth's Radiant Energy System (CERES) (Henderson et al., 2013). The biases, when compared to CERES fluxes, were determined by previous studies to fall within acceptable ranges (e.g., Henderson et al., 2013). The results 290 of sensitivity studies point to CloudSat's estimates of liquid water content (LWC) being the primary source of error in shortwave fluxes, along with the assumed properties of undetected low clouds contributing to a lesser extent (Henderson et al., 2013). On the other hand, for longwave fluxes, 295 uncertainties predominantly stem from values assigned to skin temperature and lower tropospheric water vapor (Henderson et al., 2013). Because our study region is over the North Atlantic Ocean, the variabilities in skin temperature and lower-tropospheric water vapor are expected to be smaller and, therefore, result in smaller uncertainties in the overall radiative flux estimates than when compared to those over land.

We selected radiative flux products, including derived profiles of both upwelling and downwelling 300 shortwave and longwave fluxes, along with corresponding heating profiles collocated with CALIPSO datasets for further analysis. These products comprise profiles of radiative fluxes, both with and without 305 aerosols, under clear-sky and all-sky conditions. This enables us to compute the radiative effects of aerosols and clouds in both the shortwave and longwave spectra, which we then use to estimate the influence of dust-induced changes on fluxes and the heating rate at the cloud top. The dust-induced effect is assumed to be the aerosol-induced changes over locations with pure-dust-only profiles. We use the 310 provided all-sky and all-sky no aerosol, upwelling, and downwelling fluxes to estimate the changes in radiative fluxes as follows:

$$\Delta F = F_{\text{allsky}} - F_{\text{allsky,no dust}} \quad (1)$$

Where ΔF is the change in radiative fluxes due to the presence of dust, F_{allsky} is the net (downwelling minus upwelling) flux for all-sky conditions, and $F_{\text{allsky,no dust}}$ is the same, but computed with no dust 310 (i.e., aerosol optical depth equals zero). This is estimated for both shortwave and longwave fluxes for each level given in the profile datasets. Subsequently, we calculate shortwave and longwave heating associated with the warming or cooling effect of dust as:

$$\frac{\partial T}{\partial t} = \left(\frac{1}{\rho C_p} \right) \cdot \left(\frac{\Delta F}{\Delta Z} \right)_{\text{dust}} \quad (2)$$

Where, $\frac{\partial T}{\partial t}$ is the heating rate (K day^{-1}), $\rho = 1.17 \text{ kg m}^{-3}$ density of atmospheric layer, C_p is the specific 315 heat capacity of air at constant pressure ($1004.67 \text{ J kg}^{-1} \text{ K}^{-1}$), and ΔZ is the change in vertical levels (m). Details of how these heating rate estimates are used to understand radiative responses at the low-level

cloud top, as well as used to benchmark the sensitivity analyses, are described in sections 2.2.3 and 2.2.4 below, respectively.

2.1.3 Meteorological data

320 To account for the influence of meteorological variability in our analysis, we used meteorological datasets, including temperature and humidity profiles, sea surface temperature (SST), and surface wind speed, derived from reanalysis products, such as ECMWF and MERRA-2. First, we used the CloudSat ECMWF-AUX dataset, which is an intermediate product containing ECMWF atmospheric state variables and has been interpolated to match each CloudSat CPR profile and vertical bin (Cronk, 2017). We
325 specifically used the temperature and pressure profiles from ECMWF-AUX to calculate potential temperature profiles and, subsequently, lower tropospheric stability (LTS)—an important predictor for low-level marine clouds (Wood and Bretherton, 2006). Second, to assess the large-scale influence on cloud state, we obtained other key meteorological parameters, commonly known as cloud-controlling factors (CCF), such as SST and surface wind (10 m wind), from this dataset. These CCFs have been
330 shown to influence low-level clouds over the North Atlantic region (Naud et al., 2023; Scott et al., 2020). Third, for consistency in the sensitivity analysis discussed in Section 2.2.4, we also used the profiles of temperature, pressure, and relative humidity from vertically resolved meteorological information derived
335 from the Modern-Era Retrospective Analysis for Research and Applications, Version 2 (MERRA-2) (Gelaro et al., 2017), included in CALIOP datasets as input thermodynamic profiles for simulations of radiative fluxes. The domain-averaged monthly mean profiles of temperature (dashed lines) and relative humidity (solid lines) are shown in Fig. 2c. While the temperature varies slightly, the humidity profiles show elevated relative humidity (about 50%) in the mid-troposphere that varies between May and August. While such elevated moisture could have impacts on longwave (e.g., Ryder, 2021), our methodology is
340 designed to minimize such potential meteorological effects (see section 2.2.5), and further analysis suggests that it has minimal co-variability with dust-layer characteristics over our broad selected region, which is confirmed by our results (see Section 3.5)

2.2 Analysis Procedure

We describe our methodology by first outlining the selection process for profiles with dust layers above clouds and categorizing dust-cloud configurations. Additionally, we detail the approach used to estimate

345 cloud responses to dust layer properties and estimate how cloud and meteorological variabilities may influence our findings.

2.2.1 Identification of dust above clouds

We selected profiles that contained both dust and cloud layers, specifically focusing on cases where the dust layers were found above the low-level clouds. Here, we discuss the procedure used to identify such
350 cases. First, we used feature classification flags in conjunction with the cloud layer-top and base altitude information from CALIPSO to identify locations that contained low-level clouds. For this, we focused on cases where the cloud layer-top altitude was less than 3.2 km (650 hPa) and the features were classified as clouds. To avoid multiple cloud occurrences in the same location, including the influence of high-
355 altitude clouds on low-level clouds (Christensen et al., 2013), we selected only locations with single-layer clouds from all other instances of low-level clouds. Second, we determine if these selected locations contained any dust layers. We defined cases of dust above clouds when the base of the dust layer was above the cloud-top layer by at least 200 m. Following previous studies (Kim et al., 2008; Rajapakshe et al., 2017), we used a 200 m separation between the dust-base and cloud-top layers to account for the low confidence and potential uncertainties in the CALIOP retrieved aerosol base-layer height information. In
360 addition, we excluded aerosol bases and tops extending beyond 6 km, as they are too far from the cloud top to have significant radiative effects (Herbert et al., 2020), and at these altitudes, cirrus clouds could also be misclassified as dust layers (Tackett et al., 2018). Of the approximately 292,000 profiles with single-layer low clouds examined over the 10 years (2007 to 2017) between May and August, about
365 178,000 of these profiles included dust layers. Among these 178,000 profiles, approximately 109,000 had dust layers residing above the cloud layer. The largest number of profiles having dust above the cloud is found in the eastern part of the selected domain (see Fig. S2, which also shows when aerosols are found below the cloud layer and on both sides of the cloud layers for comparison). Because our analysis further

requires the spatiotemporal collocation with the radiative flux information from CloudSat, those requirements further limit the number of available profiles that can be used (see below).

370 **2.2.2 Categorizing the dust-cloud relationship**

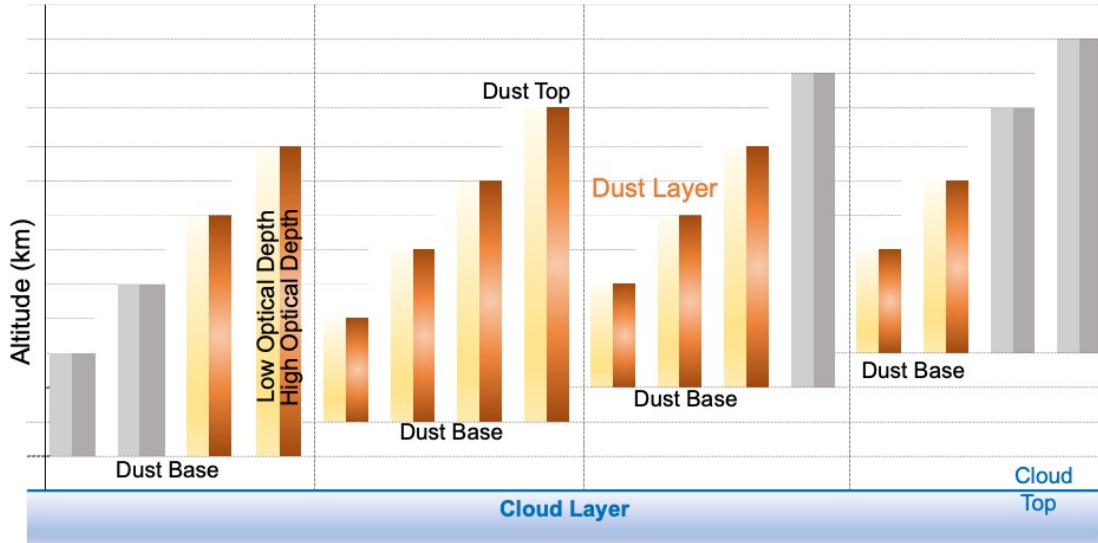


Figure 3: Schematic showing our categorization of cloud, aerosol, and radiative heating information, depending on the base and geometric thickness of the dust layer. This categorization includes dust base heights of 1, 2, 3, and 4km and geometrical thicknesses of 0.5, 1.5, 2.5, and 3.5 km, resulting in a total of 16 categories. Subsequently, each bar is split into two dust optical depth (DOD) regimes (low DOD between 0.05 and 0.2 and high DOD between 0.35 and 0.5). Gray bars do not meet the selection criteria discussed in section 2.3, thus resulting in 11 categories used for our analysis.

375

380 To understand the influence of the dust layer on the low-level cloud cover, we further divided our region of interest over the North Atlantic Ocean into $5^\circ \times 5^\circ$ grid boxes to minimize the effect of large-scale meteorological variability (Loeb and Schuster, 2008; Mauger and Norris, 2010; Scott et al., 2020). Previous studies have shown that meteorology may be confounded with aerosol-cloud interactions, even in cases where the aerosol layer is physically separated from the clouds (Arola et al., 2022; Loeb and Schuster, 2008; Mauger and Norris, 2010; Scott et al., 2020). One method for minimizing the meteorological influence on aerosol-cloud interactions is to limit the spatial region, under the assumption that meteorological conditions, including large-scale circulation, do not vary significantly within the selected region (Adebiyi and Zuidema, 2018; Loeb and Schuster, 2008). We follow Loeb and Schuster

(2008) and divide our region of interest into $5^\circ \times 5^\circ$ grid boxes. While this approach may minimize meteorological variability confounding the aerosol-cloud interactions, it limits the availability of sufficient samples for each grid box. To account for this limited sampling while still ensuring a statistically significant analysis, we developed a framework for categorizing the dust-cloud relationship within each $5^\circ \times 5^\circ$ grid box.

We categorized profiles having dust above the cloud layer in each $5^\circ \times 5^\circ$ grid box based on the dust layer base height and geometrical thickness only when aerosols, clouds, and radiative flux information are available. We stratified these profiles into four groups of dust base heights from 1, 2, 3, and 4 km, and for each of these base-height groups, we further divided them into four groups with geometrical thicknesses of 0.5, 1.5, 2.5, and 3.5 km. Therefore, within a $5^\circ \times 5^\circ$ grid box, a maximum of 16 categories can potentially exist, as illustrated in Fig. 3. To allow for robust estimates, only the $5^\circ \times 5^\circ$ grid boxes with a minimum of 30 profiles (no maximum limit) containing complete datasets of aerosol and cloud properties, meteorological parameters, and corresponding radiative fluxes were retained for further analysis. As such, not all the $5^\circ \times 5^\circ$ grid boxes contribute to each of the 16 potential dust-cloud categories in Fig. 3. For statistical significance and to determine which category to retain, we required at least six $5^\circ \times 5^\circ$ grid boxes over the North Atlantic Ocean to meet the minimum 30-profile requirements to be averaged for each dust-cloud category. Therefore, the minimum number of profiles required for each dust-cloud category of Fig. 3 is at least 180 profiles, limiting the final number of categories to 11 distributed across the groups of dust base heights and geometric thicknesses (gold/golden brown bars in Fig. 3). These 11 dust-cloud categories still allow for the comparison of average cloud responses based on dust layers characteristics of geometrical thickness and base heights. We used this categorical method to account for potential cross-correlation between predictors (such as dust geometric thickness, base height, and optical depth), which would otherwise require calculating interaction terms in a multilinear regression, and to avoid potential nonlinearities and negative impacts of outliers, allowing us to isolate the impact of each parameter while maintaining statistical robustness through sample size criteria. Because dust layers with the same geometrical thickness or base heights can exhibit varying dust optical depth, we further divided our

415 categories into cases of low and high optical depth with values between 0.05-0.2 and 0.35-0.5, respectively (see Fig. 3).

2.2.3 Estimating cloud and radiation responses to dust-layer characteristics

To understand the response of the low-level cloud cover to above-cloud dust characteristics, we first computed grid-normalized cloud fraction obtained from CALIPSO and CloudSat separately for each of
420 the 11 categories within every participating $5^\circ \times 5^\circ$ grid box, using the following expression:

$$f' = \frac{\bar{f}_{cat}(x, y)}{\bar{f}_{lowcld}(x, y)} \quad (3)$$

Where $\bar{f}_{cat}(x, y)$ is the mean low-level cloud cover corresponding to each category at each grid box (x-longitude and y-latitude), and $\bar{f}_{lowcld}(x, y)$ is the grid mean values averaged for the time period (May-August, 2007-2017). We used normalized cloud fraction for each category because of instrumentation
425 differences in CloudSat and CALIPSO and because retrieval of these cloud variables is not done using a similar approach, and as such, their values are not consistent for the same longitude and latitude grid, as similarly highlighted by previous studies (e.g., Bertrand et al., 2024; Kahn et al., 2008). For example, CloudSat often underestimates low-level cloud cover due to its “surface clutter” zone, meaning it cannot detect clouds very close to the ground, often common over the ocean, while CALIPSO’s lidar can detect
430 thin, low-lying clouds that CloudSat might miss, leading to a higher low-level cloud fraction measurement from CALIPSO (Bertrand et al. 2024). Therefore, normalizing the cloud fraction estimates allows us to compare changes in cloud fraction to changes in dust layer characteristics (cloud fraction response) and helps us understand whether such cloud sensitivity is robust across different datasets. In addition, although
435 not included in this paper, we also analyzed other similar properties, such as cloud optical depth, for each category, with similar conclusions to cloud fraction.

We used the variation in f' across the categories to calculate cloud responses to changes in the dust-layer base height, geometrical thickness, and dust optical depth. Specifically, we define estimating low-level cloud response as the rate of change of grid-normalized cloud fraction per unit change in dust base height
440 ($\frac{\partial f'}{\partial DBH} \Big|_{DGT}$) and geometric thickness ($\frac{\partial f'}{\partial DGT} \Big|_{DBH}$), when the other parameter is held constant. This can be visualized as the difference in grid-normalized cloud fraction in Fig. 3 as the geometrical thickness increases from left to right (for fixed base height) or as the dust-layer base height increases from left to right (for the same geometric thickness). In addition, similar low-level cloud responses can also be estimated for dust optical depth.

Similar to cloud fraction, we categorized the relevant radiative fluxes and associated all-sky and dust-induced heating for each dust-cloud category. Specifically, we computed the radiative heating rate within
445 the dust layer and at the cloud tops, as well as all-sky radiative fluxes for shortwave and longwave

radiation at cloud tops for each category shown in Fig. 3. Similar to cloud response, we estimate the dust-induced cloud-top heating rate responses to a unit increase in dust base height ($\left(\frac{\partial CldTopHt_{dust}}{\partial DBH}\right|_{DGT}\right)$ and geometric thickness ($\left(\frac{\partial CldTopHt_{dust}}{\partial DGT}\right|_{DBH}\right)$).

450 2.2.4 Separating dust impacts from the cloud properties and underlying thermodynamic profiles

Although radiative heating estimates from CALIPSO–CloudSat products help establish the link between dust-induced cloud top heating and cloud response, the heating rate also depends on factors such as single-particle properties (e.g., extinction efficiency, single scattering albedo, asymmetry parameter) and the background temperature and humidity profiles. Moreover, dust-layer radiative heating is highly sensitive 455 to absorption properties, such as particle size distribution and complex refractive index. For instance, dust layers dominated by coarse particles may exhibit stronger in-layer longwave cooling compared to those dominated by finer particles. In addition, distinct average thermodynamic profiles (of temperature and humidity) across categories (see Fig. S3) could also influence cloud-top radiative cooling and confound the observed dust-induced changes in cloud-top radiative cooling. Additionally, differences in cloud 460 properties across categories may drive variations in cloud-top cooling independent of dust effects. Thus, to isolate the influence of dust properties, cloud properties, and thermodynamic profiles, we conducted sensitivity experiments using the Santa Barbara DISORT Atmospheric Radiative Transfer (SBDART) model (Ricchiazzi et al., 1998). SBDART is a widely used radiative transfer model that solves solar and thermal infrared radiation using the DISORT (Discrete Ordinates Radiative Transfer) algorithm. It allows 465 the specification of surface types (e.g., ocean, desert, snow, forest) and user-defined atmospheric profiles for temperature, humidity, and pressure. The model also incorporates cloud parameters such as optical depth, cloud-top height, phase, and effective radius, enabling detailed simulation of radiative fluxes within and around cloud layers.

Using SBDART, we first recreate CloudSat-CALIOP radiative fluxes for each dust–cloud category in 470 Fig. 3 using associated retrieved dust extinction profiles, cloud properties, and temperature and humidity profiles, for the time close to CALIPSO passes, that is, about 15:00 UTC, over the selected study region. The average atmospheric and dust/cloud properties for each category are shown in Fig. S3a & b and Table 475 S1, including dust optical depth, cloud optical depth, and cloud top/bottom heights. To calculate single-particle optical properties (extinction coefficient, single scattering albedo, and asymmetry parameter), we applied Mie theory (Wiscombe, 1980), assuming spherical dust particles, using particle volume size distributions (Fig. S4a) and spectrally resolved complex refractive indices (Fig. S4b & c).

We considered three types of dust size distributions based on the measurements first collected by (Adebiyi and Kok, 2020) and recently standardized by Formenti and Di Biagio, 2024: first, a distribution typical

of source regions with \approx 89% coarse-mode particles ($>2.5\text{ }\mu\text{m}$, Source - magenta line in Fig S4a); second, 480 a medium-range transported case with \approx 83% coarse-mode (MRT - red line in Fig S4a); and third a long- range transported case dominated by fine particles (\approx 50% coarse-mode, LRT; blue line in Fig S4a). To 485 capture variability in absorption due to dust aging, we used refractive indices from Di Biagio et al. (2019), OPAC (Hess et al., 1998), and Volz, 1972, with shortwave imaginary refractive indices of 0.0026, 0.0075, and 0.0080 at $0.5\text{ }\mu\text{m}$ wavelength, and longwave values of 0.3534, 0.4783, and 0.1620 at $10\text{ }\mu\text{m}$ wavelength (Fig. S4b & c). These combinations yield nine cases with spectrally varying extinction 490 efficiency, single scattering albedo, and asymmetry parameter, which we used as inputs to SBDART to examine how cloud-top heating responds to changes in dust size and absorptive properties (Fig. S4d, e & f). We computed radiative fluxes for shortwave ($0.25\text{--}4\text{ }\mu\text{m}$), longwave ($4\text{--}40\text{ }\mu\text{m}$), and the total ($0.25\text{--}40\text{ }\mu\text{m}$) corresponding to each category based on average values of temperature and humidity profiles, 495 aerosols, and cloud parameters. From these calculated radiative flux profiles, we estimated dust-layer and cloud-top heating/cooling rates, and the influence of dust on cloud-top heating/cooling rates.

To isolate the effects of dust properties, cloud properties, and thermodynamic profiles on cloud-top 500 radiative cooling, we performed 431,000 radiative transfer simulations using the SBDART model. These simulations were conducted using solar zenith angles corresponding to the approximate local time of CALIPSO overpasses (\sim 15:00 UTC) in the study region. As such, the radiative fluxes represent near- 495 instantaneous conditions at the time of satellite observations, not daily averages. These simulations are performed for a combination of 11 thermodynamic (temperature and humidity) profiles, 11 dust structural categories (including dust-layer geometric thickness and base height), 11 cloud optical depths, and 11 dust optical depths, across three spectral bands: shortwave ($0.25\text{--}4\text{ }\mu\text{m}$), longwave ($4\text{--}40\text{ }\mu\text{m}$), and total 500 ($0.25\text{--}40\text{ }\mu\text{m}$). We used 9 combinations of single-particle dust properties, resulting in 395,307 simulations. Additionally, we conducted 35,937 simulations with zero dust optical depth to calculate dust- 505 induced radiative heating profiles (as in equations 1 and 2 above). From these profiles, we estimated all-sky and dust-free sky cloud-top cooling, as well as dust-induced heating at the cloud-top for all three spectral bands. Since we used different dust-particle optical properties than those used in deriving CALIPSO-CloudSat fluxes, we normalized the observed and simulated dust-induced cloud-top heating by their 510 respective mean across categories to enable meaningful comparisons. We further calculated the sensitivity of dust-induced cloud-top heating to dust layer geometric thickness and base height using both the normalized CloudSat-CALIPSO-derived heating and normalized SBDART-simulated heating.

To understand the dominating factors in dust-induced cloud-top heating, we quantified the sensitivity of 510 heating rates to dust layer geometric thickness and base height under three controlled experimental setups (see Table S1). First, we isolated the effect of dust properties on cloud-top heating rates by allowing the dust optical depth and dust structural category to vary across simulations, while holding the cloud optical depth and thermodynamic profiles fixed. The resulting sensitivities reflect the influence of dust optical

515 properties alone, evaluated across 121 combinations of fixed values (11 cloud optical depth \times 11 thermodynamic profiles; see experiment-2 in Table S1). Second, we isolated the effect of cloud properties on cloud-top heating rates by fixing dust optical depth, thermodynamic profiles, and dust structural category, and varying cloud optical depth and cloud top height, resulting in 1331 combinations (11 dust optical depth \times 11 dust categories \times 11 thermodynamic profiles; see experiment-3 in Table S1). Third, we assess the role of the thermodynamic profile by fixing dust optical depth, cloud optical depth, and dust category, and allowing only the thermodynamic profiles to vary, again producing 1,331 combinations (see experiment-4 in Table S1). As discussed earlier, to enable meaningful comparison across simulation setups, we normalized all simulated dust-induced cloud-top heating values using the mean heating from the full simulation set, where dust properties, cloud properties, and thermodynamic profiles were all allowed to vary. We then used these three sets of normalized cloud-top heating values to estimate the 520 sensitivities of cloud-top heating rates to geometric thickness and dust base height, attributed specifically to the effects of dust properties, cloud properties, or thermodynamic profiles, thereby enabling a robust diagnosis of their contributions to dust-induced cloud-top heating rates.

2.2.5 Quantifying the role of dust particle size and absorption

530 To examine how particle size distribution and refractive index influence dust-induced cloud-top heating, we calculated all-sky, no-dust, and dust-induced heating for all nine combinations (Fig. S4) of dust single-particle optical properties, derived from three representative size distributions, source-region dominated (89% coarse-mode), medium-range transported (83% coarse-mode), and long-range transported (50% coarse-mode), and three sets of spectrally varying complex refractive indices (from Di Biagio et al., 2019; OPAC, Hess et al., 1998; and Volz, 1972). For each combination, we computed the sensitivity of dust-induced cloud-top heating to dust optical depth under fixed cloud optical depth, cloud-top height, and thermodynamic profiles. These simulations quantify how different dust compositions, characterized by varying absorption and scattering efficiencies, modulate the radiative impact of dust layers on low-level clouds. The resulting nine dust optical depth sensitivities help estimate the effect of size and dust-longwave absorptivity.

540 2.2.6 Estimating the influence of meteorology

In tropical and subtropical oceanic regions, meteorological factors commonly known as cloud-controlling factors, such as sea surface temperature (SST), inversion strength, subsidence, and surface wind speed, influence the cloud cover (Klein et al., 2017; Scott et al., 2020). For example, a higher SST typically leads to an expansion of the boundary layer heights, reducing cloud formation and persistence, while 545 stronger inversion strength limits dry air entrainment, promoting larger cloud cover. Subsidence, often quantified using vertical velocity at 700 hPa or adjacent layers above the cloud (Adebiyi et al., 2015;

Naud et al., 2023), generally correlates positively with cloud fraction. However, when inversion strength is constant or absent, stronger subsidence may reduce cloud cover (Adebiyi and Zuidema 2018). Similarly, surface wind speed, a frictional driver of evaporation, theoretically should lead to an increase 550 in cloud fraction with enhanced wind speed. Nevertheless, wind speed is also tied to temperature and moisture advection, resulting in an unclear relationship with cloud cover. Thus, it becomes necessary to analyze these cloud-controlling factors to establish the causal effect of dust on low-level clouds. As highlighted above, to minimize the effect of such cloud-controlling factors in our analysis, we restricted 555 our analysis to small grid boxes ($5^\circ \times 5^\circ$ grid box), where we assume meteorological variability is largely invariant and considered the same season.

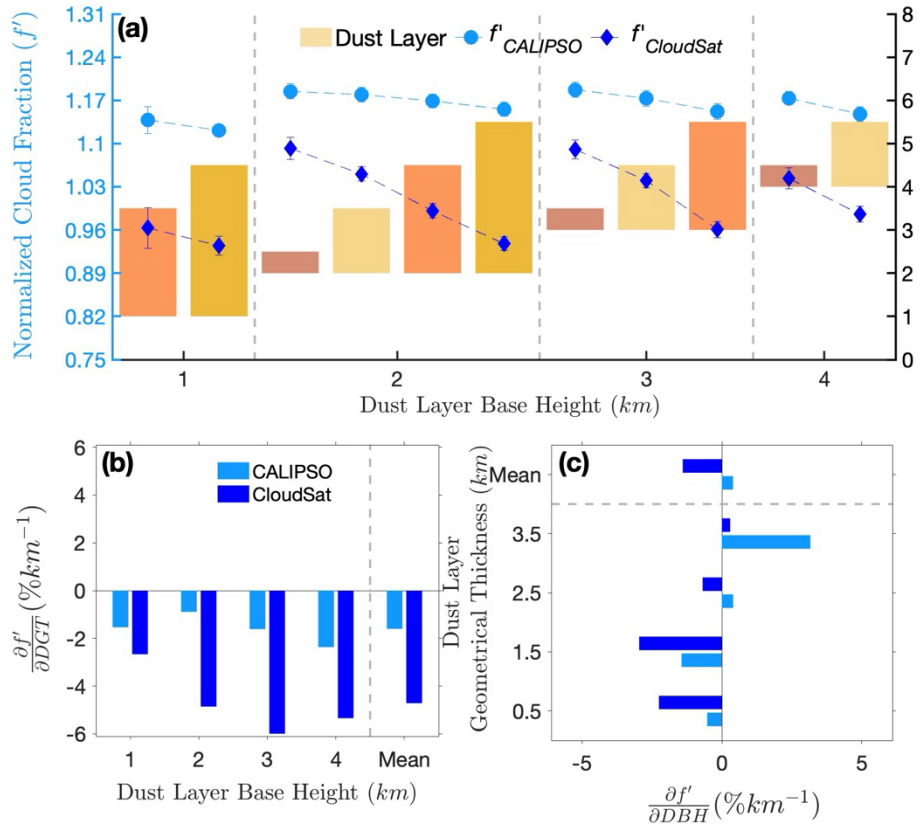
Further, to understand the effect of these confounding meteorological variables, we compared the anomalies of these cloud-controlling factors, such as surface wind speed, sea-surface temperature, inversion strength, and humidity, across the categories in Fig. 3 (see Fig. S5 for respective spatial 560 patterns). A negligible and non-systematic variation in these parameters across the categories would suggest their minimal influence on estimated low-level cloud responses. For example, the radiative response of above-cloud humidity, which can affect the cloud by entraining into the cloud layer and can increase downwelling longwave radiation reaching the cloud top, may resemble the longwave effect of dust and could be difficult to separate from the radiative effect of above-cloud dust. We adopted an 565 approach discussed by Eastman and Wood (2018) to estimate the entraining humidity, defined as specific humidity in the layer directly above the inversion top, and the radiating humidity, defined as the mean humidity above the inversion top and below 700 hPa. The inversion top in the present study was considered a layer just above the cloud top instead of being estimated from the potential temperature profile. Though this is a simplified definition of the inversion top and may not fully apply to clouds with cumulus characteristics, here, we are mainly interested in moisture available for entraining into cloud.

570 3 Results

We found that low-level clouds are sensitive to the dust-layer altitude, geometric thickness, and dust 575 optical depth over the North Atlantic, and this sensitivity is associated with the longwave radiation induced by the above-cloud dust layer. The details of these results are presented below, including in Section 3.1, where we discuss the cloud response to changes in dust base height (DBH) and geometric thickness (DGT); Section 3.2, where we isolate the influence of dust optical depth (DOD) on these cloud responses for each combination of DBH and DGT, and Section 3.3 where we estimate the contributions of the DBH, DGT, and DOD to low-level cloud response. In Section 3.4, we explain how the perturbations in these dust characteristics (DBH, DGT, and DOD) affect cloud-top radiative fluxes and, consequently, modify cloud-top longwave cooling that facilitates the observed changes in the low-level cloud cover. 580 Finally, we examine in Section 3.4 the role of meteorological variability that may affect the instantaneous

radiative heating rates and the large-scale environment that may confound with the influence of dust characteristics on the low-level cloud response.

3.1 Low-level cloud response to dust layer characteristics.



585 **Figure 4: Variation and response of low-level grid-normalized cloud fraction to the geometrical
590 thickness and dust layer base.** (a) The mean grid-normalized cloud fractions (f') for CALIPSO
595 and CloudSat (circular and diamond markers, respectively) for each category defined in Figure 3
(see section 2.2.3 for details). The bars represent categories with the same base height group, and
those with the same geometric thickness are represented by the same colors across the different
groups. The height of the bars corresponds to geometrical thickness: 0.5 km (violet), 1.5 km (light
yellow), 2.5 km (orange), and 3.5 km (yellow) at the dust-layer base of 1, 2, 3, and 4 km. Error bars
indicate the standard error. (b) Low-level cloud response to dust-layer geometrical thickness
 $\left(\frac{\partial f'}{\partial DGT}; \%\ km^{-1}\right)$, shown for different dust-layer base heights. (c) Low-level cloud response to dust
base height $\left(\frac{\partial f'}{\partial DBH}; \%\ km^{-1}\right)$ for different geometrical thicknesses. Light blue bars represent the
595 low-level cloud response for CALIPSO, and dark blue bars are for CloudSat.

As shown by previous studies (e.g., DeFlorio et al., 2014; Doherty and Evan, 2014) and highlighted earlier in Fig. 1d, low-level cloudiness typically increases due to dust's semi-direct effect over the North Atlantic Ocean when the dust is above the cloud layer. However, here, we found that the extent of this increase
600 also depends on the dust layer's relative altitude and geometrical thickness. To understand this relationship, we categorized the low-level cloud fraction based on dust base height (DBH) and dust geometric thickness (DGT), and the resulting categories are shown in Fig. 4a for grid-normalized cloud fraction (f') – the cloud fraction for each category normalized by the climatology over each grid box – for CloudSat and CALIPSO (see section 2.2.3 above). The result shows that the domain-mean grid-
605 normalized cloud fraction (f') is greater than unity for CALIPSO and CloudSat (1.16 (± 0.12) and 1.01 (± 0.27), respectively). As highlighted earlier (see section 2.2.3), the difference between estimate of cloud fraction in CloudSat and CALIPSO is likely associated with differences in instrumentation (radar versus lidar), resulting in different limitations and uncertainties in the retrieved cloud fraction, including underestimation of CloudSat low-level cloud cover due to its difficulty to detect clouds very close to the
610 ocean surface (e.g., Bertrand et a. 2024).

Despite this difference in retrieved cloudiness, the cloud cover decreases as a function of dust-layer geometric thickness, regardless of the dust-base altitude, in both datasets. Specifically, when the dust-base height is 1 km, for an increase of geometric thickness from 2.5 km to 3.5 km, the reduction in grid-normalized cloud fraction ranges by about 1% (1.13 to 1.12) for CALIPSO and about 3 % (0.96 to 0.93)
615 for CloudSat. Similarly, when the dust-base height of 2 km and dust-layer geometric thickness increases between 0.5 and 3.5 km, the reduction in grid-normalized cloud fraction ranges by about 3% (from 1.18 to 1.15) for CALIPSO and about 16% (1.09 to 0.93) for CloudSat (see Fig. 4a). When the dust-base height is 3 km (geometric thicknesses between 0.5 and 2.5 km) and at 4 km (geometric thicknesses between 0.5 and 1.5 km), the reduction in the grid-normalized cloud cover ranges by about 3% and 3% for CALIPSO
620 and 13% and 6% for CloudSat, respectively. Overall, all categories of dust base height and geometric thickness show a reduction in grid-normalized cloud fractions, but the ranges of the reduction for CloudSat are consistently larger than those for CALIPSO, indicating the much larger variability in CloudSat low-level cloud fraction over the North Atlantic Ocean. Although the magnitudes of these changes in cloudiness are small, they are statistically significant and indicate that changes in dust-layer geometric thickness influence low-level cloudiness.
625

Because the classes of dust-layer geometric thickness are not the same for the different dust-base altitudes (see Fig. 3 & Fig. 4a), we further isolate the cloud response to changes in dust-base height, separate from the geometric thickness by examining how the grid-normalized cloud fraction changes per unit change in one parameter while holding the other relatively constant (Fig. 4b & c). The result shows that a unit

630 increase in dust-layer geometric thickness consistently leads to a reduction in cloudiness regardless of the dust-base height (Fig. 4b). On average, cloud fraction decreases by 1.7% and 5.1% for each kilometer increase in dust-layer geometric thickness based on CALIPSO and CloudSat, respectively (see the last bars in Fig. 4b). Additionally, the low-level cloud response to a unit change in geometric thickness is stronger for higher dust-base altitudes. Specifically, for each kilometer increase in geometric thickness, 635 the low-level cloud response is -1.54%, -0.89%, -1.16%, and -2.37% for dust layers with base heights of 1 km, 2 km, 3 km, and 4 km, respectively, for CALIPSO and are -2.66%, -4.86%, -5.99%, and -5.34% for CloudSat.

In addition, the grid-normalized low-level cloud response to one unit change in dust-base height depends 640 on the dust-layer geometric thickness. For relatively thinner dust layers ($DGT \leq 1.5$ km), we find that an increase in dust-base height tends to decrease cloud fraction. Conversely, for relatively thicker dust layers ($DGT \geq 2.5$ km), we find that an increase in dust-base height results in an increase in cloud fraction (see Fig. 4c). Although this inference is generally consistent with varying magnitude across the datasets, for a 645 geometric thickness of 2.5 km, the cloud response to changes in dust-base height is negative for CloudSat. Specifically, the low-level cloud response is positive (0.40%/km) in CALIPSO but negative (-0.69%/km) in CloudSat. In addition, for dust-layer geometric thickness greater than ≈ 3.5 , the cloud response in 650 CALIPSO is substantially larger than that of CloudSat, although of the same sign. These inconsistencies may be attributed to the differences in retrieved cloud fraction between CALIPSO and CloudSat, resulting in different variabilities that are exacerbated by the selection procedure (see e.g., Fig. S6). Overall, for thinner dust layers, a unit increase in dust-layer base height reduces cloud cover by 0.52% and 1.44% for geometric thickness values of 0.5 km and 1.5 km, respectively, using CALIPSO data and 2.25% and 2.95%, respectively, using CloudSat. In contrast, for thick dust layers ($DGT=3.5$ km), increasing the dust base height leads to an increase in cloud response, with values of 3.17% and 0.30% from CALIPSO and CloudSat data, respectively.

3. 2 Influence of dust optical depth in cloud response to dust layer characteristics.

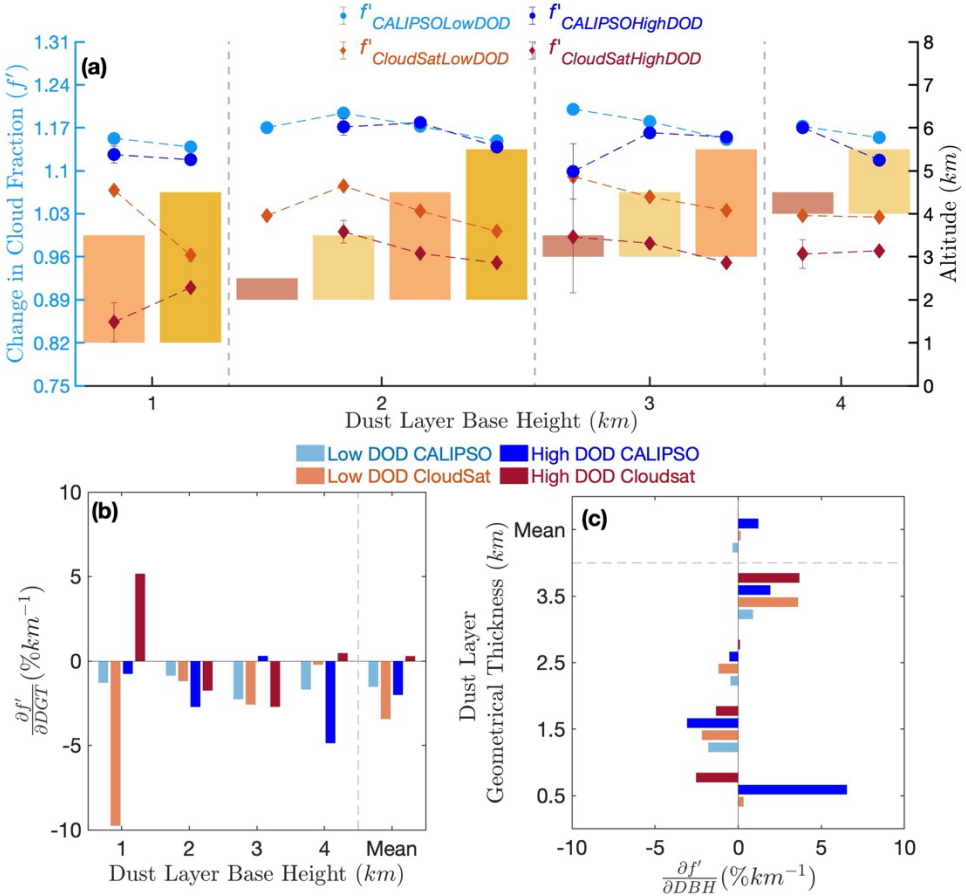


Figure 5: (a) The mean grid-normalized cloud fraction (f') separated into low (0.05–0.2; $\mu \pm \sigma = 0.12 \pm 0.02$; light blue and light red lines) and high (0.35–0.5; $\mu \pm \sigma = 0.41 \pm 0.02$; dark blue and dark red lines) dust optical depth (DOD) for the categories defined in Fig. 3. Circular markers with blue colors are for CALIPSO, and diamond markers with red colors are for CloudSat. The bars represent categories with the same base height group, and those with the same geometric thickness are represented by the same colors across the different groups. The height of the bars corresponds to geometrical thickness: 0.5 km (violet), 1.5 km (light yellow), 2.5 km (orange), and 3.5 km (yellow) at the dust-layer base of 1, 2, 3, and 4 km. Error bars indicate the standard error. (b & c) Low-level cloud response to (b) dust layer geometrical thickness and (c) dust base heights separated for low and high DOD cases. Blue bars are for CALIPSO, and red bars are for CloudSat. Light colors show responses corresponding to low DOD values, while dark colors are for high DOD.

Because dust-base altitude and geometric thickness may also co-vary with dust optical depth (DOD), we further divided our categories (shown in Fig. 4a) into subsets based on profiles with low (0.05–0.2; $\mu \pm \sigma = 0.12 \pm 0.02$) and high (0.35–0.5; $\mu \pm \sigma = 0.41 \pm 0.02$) DOD values (see Fig S7) and estimated the corresponding grid-normalized cloud fraction (see Fig. 5a). We find that the variations in cloud fraction

as a function of dust-base height and geometric thickness for both low and high DOD cases broadly remain consistent with the patterns observed for all dust (compare Fig. 5a and Fig. 4a). Specifically, the 675 cloud fraction generally decreases as geometric thickness increases. Additionally, the grid-normalized cloud fractions for the same category are usually lower for high DOD cases than for low DOD cases. This suggests that cloud fraction responds negatively to increases in DOD, contrasting with the cloud response to biomass-burning aerosols that show an increase with higher aerosol optical depth (Adebiyi and Zuidema, 2018). In other words, while cloud response to DOD typically results in enhancement of low-level 680 cloudiness (i.e., cloud response to above-cloud dust semi-direct effect; as shown in Fig. 1d and Fig. 4a), that enhancement decreases as DOD increases, with stronger enhancement occurring for low DOD than high DOD cases. When averaged across all categories, the mean grid-normalized cloud fraction differs between low and high DOD cases by about 3% (1.17 ± 0.02 and 1.14 ± 0.02) for CALIPSO and about 9% (1.04 ± 0.04 and 0.95 ± 0.04), respectively.

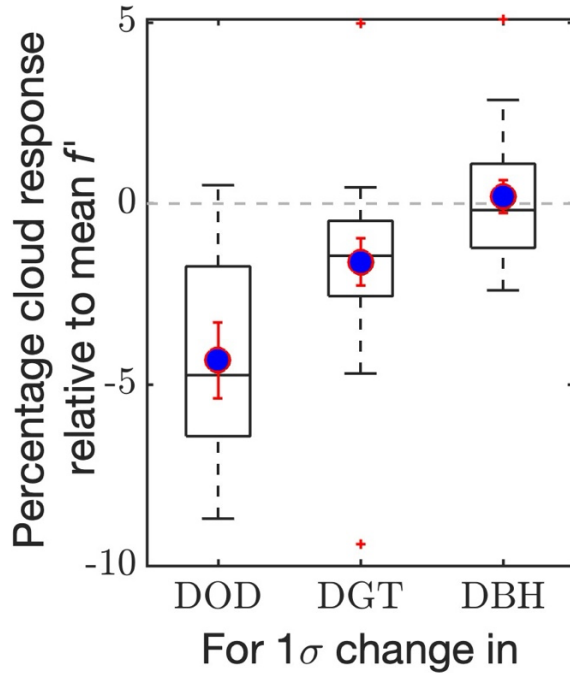
Furthermore, we also find that the cloud fraction decreases with increasing DOD and is broadly consistent 685 regardless of the range used to define low and high DOD cases. Specifically, we find negative low-level cloud changes to increasing DOD are consistent across all combinations of dust-base height and geometric thickness (e.g., Fig. S8). Consequently, we estimate cloud response to DOD as the change in grid-normalized low-level cloud fraction per unit change in DOD (Fig. S8). The result shows that the mean low-level 690 cloud fraction changes by approximately -17 % per unit change in DOD. Similarly, the cloud response to DOD ranges from -81% to +2%, depending on the combination of dust-layer base altitude and its geometric thickness (see Fig. S8). While low-level cloud cover is sensitive to increases in DOD, the results suggest that potential co-variabilities between dust-layer characteristics and DOD do not significantly influence the cloud response to dust-base height and geometric thickness.

Therefore, we separate the influence of dust-base height and geometric thickness on low-level clouds for 695 low and high DOD cases (Fig. 5b & c; as done above in Fig. 4b & c). Our result shows that the low-level cloud response to dust-layer geometric thickness ($\frac{\partial f'}{\partial GT}$) is stronger for high DOD cases, despite having lower grid-normalized cloud fraction, than for low DOD cases (Fig. 5b). The mean cloud responses to geometric thickness are $-1.53\%/\text{km}$ and $-2.01\%/\text{km}$ of the mean f' for low and high DOD cases, respectively, for CALIPSO. In contrast, for CloudSat, the mean cloud response to geometric thickness is 700 stronger for low-DOD cases (-3.44%) compared to high-DOD cases (0.29%). However, this difference in CloudSat, when compared with CALIPSO, is because of the large variation in cloud response for the dust layer at 1 km base (see first column in Fig. 5b). Removing that extreme case, our results show consistency between CloudSat and CALIPSO and indicate that the low-level cloud response to geometric thickness remains negative for low and high DOD cases. Unlike the low-level cloud response to 705 geometric thickness, the mean cloud response to dust-base height ($\frac{\partial f'}{\partial DB}$) is relatively small due to

contrasting signs for low and high DOD cases (Fig. 5c). For CALIPSO, the mean cloud responses are -0.34% for low DOD and 0.14% for high DOD, and, for CloudSat, the mean responses are 1.22% for low DOD and -0.02% for high DOD.

3.3 Contributions of dust-layer characteristics and optical properties to low-level cloud

710 response



715 **Figure 6: Box-and-whisker plot showing the percentage change in cloud response relative to the mean f' for a 1σ (1 standard deviation) change in dust optical depth (DOD; $1\sigma = 0.27$), geometric thickness (DGT; $1\sigma = 0.964$ km), and dust base height (DBH; $1\sigma = 0.778$ km). Blue markers represent the mean values, with error bars indicating the standard error (red).**

Because of the different units in the cloud response to dust-layer characteristics (dust base height, DBH, and dust geometric thickness, DGT) and dust optical depth (DOD), it is difficult to assess their relative contributions to the low-level cloud responses. To understand the relative contribution of dust-layer DGT, DBH, and DOD, we estimate the sensitivity in the low-level cloud response to a one-standard-deviation

720 (1σ) increase in each parameter relative to the basin-wide mean cloud fraction ($\sigma_x \frac{\partial f'}{\partial x}$; where X is DOD, DGT or DBH and σ_x is their standard deviations). As shown above, and for one unit change in each parameter (DOD, DGT, and DBH), the low-level cloud responds negatively with the strongest cloud response to the unit change in DOD (see Fig. 6). Specifically, we find that relative reduction in cloud

725 response to 1σ change in DOD is about $-4.3 (\pm 1.04) \%$, compared to $-1.6 (\pm 0.65) \%$ and $0.19 (\pm 0.45) \%$
730 to 1σ change in dust-layer geometric thickness and dust base respectively. In other words, if all parameters remain constant, a 1σ change in DOD will reduce the low-level cloud fraction by about a factor of 3 more than a 1σ change in DGT, and significantly more than a 1σ change in DBH that is largely negligible within the error range. Overall, our results, examining the effects of dust base heights, dust geometric thicknesses, and dust optical depth on low-level cloud cover, indicate that low-level clouds respond negatively to increases in all three considered dust properties and characteristics, but more strongly to increases in dust optical depth and geometric thickness than to the same increases in dust base height.

3.4 Radiative influence of dust-layer characteristics and optical properties on low-level cloudiness

735 We hypothesize that the variations in radiative fluxes at the cloud top drive the observed cloud responses to perturbations in dust-base heights, geometric thickness, and dust optical depth. This hypothesis builds on the traditional mechanism of aerosol semi-direct effect, whereby changes in cloud response to above-cloud absorbing aerosols occur through radiative influence at cloud-top, such as changes in cloud-top entrainment (Wilcox, 2010). As highlighted in the introduction (section 1), the mechanisms of dust semi-740 direct effect are expected to deviate from traditional mechanisms associated with other absorbing aerosols, such as black carbon, because the pathways of dust-radiation interactions now include the longwave radiation that is generally absent in other absorbing aerosols. Within this context, therefore, we seek to understand the radiative influence of dust layer characteristics on low-level cloudiness. To do so, we examined how changes in dust base heights, dust geometric thickness, and dust optical depth influence radiative heating rates within the dust layer and at the underlying low-level cloud top, and consequently, 745 the relationship with the low-level cloudiness.

3.4.1 Changes in dust-induced radiative impacts due to dust layer characteristics

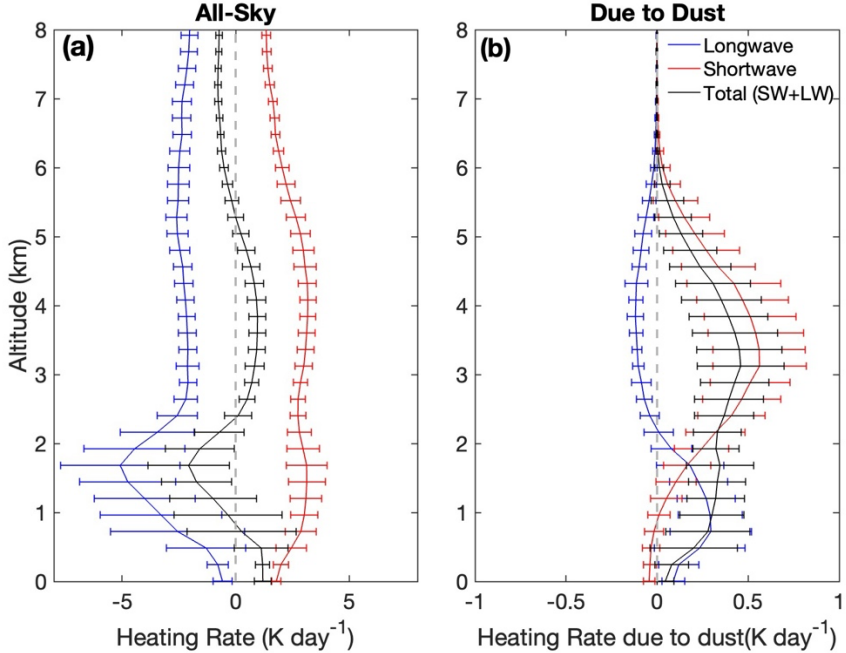


Figure 7: The domain-mean heating rate profiles over the North Atlantic Ocean for (a) all-sky and (b) due to dust, calculated from the difference between all-sky with and without dust radiative fluxes (see section 2.1.2). Red lines are shortwave (SW) heating rates, blue lines are longwave (LW) heating rates, and black is total (SW+LW). Error bars indicate the standard deviation for each level.

Using the CALIPSO-CloudSat heating rates profile averaged over the North Atlantic Ocean (see box in Fig. 1), Fig. 7 shows that the dust layer above the low-level cloud is well-defined between approximately 2.5 and 6 km with dust-induced total radiative warming at the low-level cloud top. Within the dust layer, the all-sky shortwave warming dominates the longwave cooling in the total heating rates (Fig. 7a). In addition, these all-sky heating rates are primarily because of the dust-radiation interaction within the layer, which shows levels of maximum longwave emission slightly above levels of maximum shortwave extinction (Fig. 7b). Specifically, the peak dust-induced shortwave warming of $0.56 (\pm 0.26)$ K day $^{-1}$ occurs at approximately 3.12 km, whereas dust-induced longwave cooling peaks at approximately 3.82 km with a value of $-0.12 (\pm 0.04)$ K day $^{-1}$ (Fig. 7b).

In contrast to the dust layer, the all-sky total heating rates within the boundary layer are dominated by longwave cooling, and slightly opposed by shortwave warming, close to the cloud top as expected for low-level clouds (Fig. 7a). However, we find that the presence of dust layer above the cloud induces an anomalous longwave warming reinforcing the all-sky shortwave warming and counteracting the mean longwave cooling within the boundary layer. In other words, dust-induced longwave warming effectively

weakens the total cloud-top radiative cooling when dust is present above the low-level clouds than when it is not. In addition, this anomalous dust-induced longwave warming peaks at approximately 0.72 km with a value of $0.30 \pm 0.22 \text{ K day}^{-1}$ (Fig. 7b). Overall, the profiles show that dust-induced shortwave warming dominates total heating rates within the dust layer and dust-induced longwave warming weakens the dominant mean longwave cooling within the boundary layer. It is also worth noting that the uncertainties in the total heating rates are dominated by the uncertainties in shortwave heating rates within the dust layer and the uncertainties in the dust-induced longwave heating rates within the boundary layer (see error bars in Fig. 7).

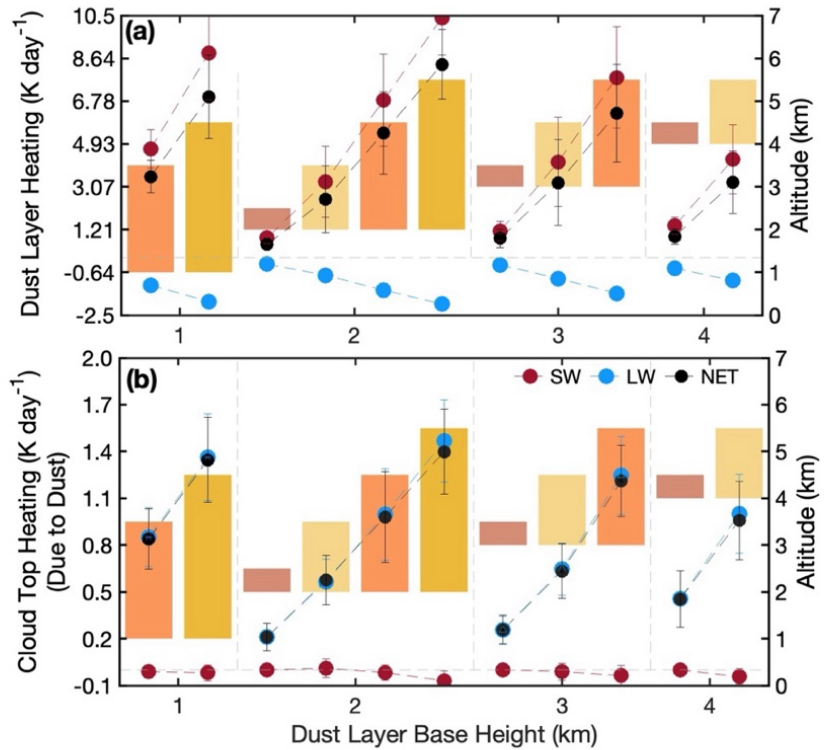
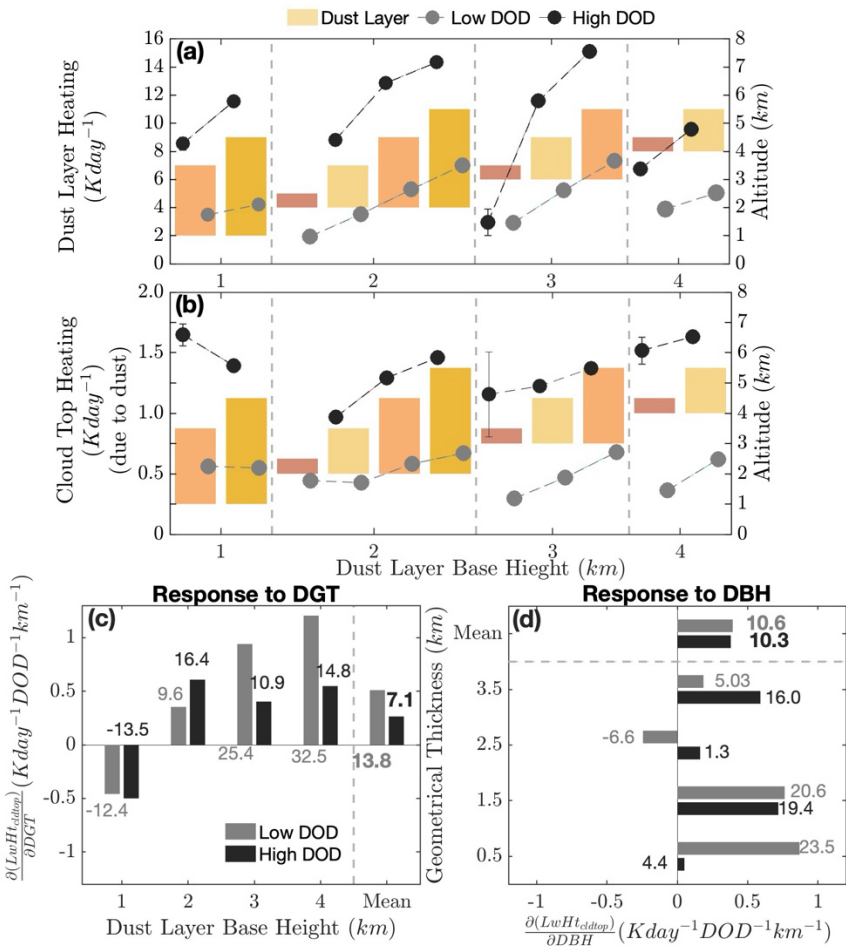


Figure 8: Dust-induced radiative heating (a) within the dust layer and (b) at the low-level cloud top, separated into categories based on dust-layer base height and geometric thickness. Dashed lines are the radiative heating rates of shortwave (SW; red lines), longwave (LW; blue lines), and total (SW+LW; black lines). The bars represent categories with the same base height group, and those with the same geometric thickness are represented by the same colors across the different groups. The height of the bars corresponds to geometrical thickness: 0.5 km (violet), 1.5 km (light yellow), 2.5 km (orange), and 3.5 km (yellow) at the dust-layer base of 1, 2, 3, and 4 km. Error bars indicate the standard error.

Separating the heating rates as a function of the dust-layer characteristics, we find that changes in the dust-induced heating or cooling rates within the dust layer and within the low-level clouds vary as a function of the geometric thickness of the dust layer (Fig. 8 and Fig. S9). Specifically, our results indicate
790 that dust-induced shortwave warming continues to dominate over longwave cooling within the dust layer, with both strengthening with increasing geometric thickness of the dust layer (Fig 8a). Between the dust-
layer categories, the mean all-sky shortwave heating within the dust layer as a function of geometric thickness ranges up to about 10.3 K day^{-1} , partially offset by the mean longwave cooling that can also range up to 2.01 K day^{-1} (e.g., for a dust base height of 2 km in Fig. 8a). In addition, for each category,
795 the shortwave heating peaks around the middle of the dust layer whereas the longwave cooling peaks slightly above it (Fig S9), similar to the basin-wide mean profiles in Fig. 7. In contrast to the dust layer, dust-induced longwave warming within the low-level cloud dominates over the dust-induced shortwave cooling, which results from increased longwave downwelling radiation emitted by the dust layer and the reduction of solar radiation reaching the cloud top due to attenuation by the overlying dust. The total
800 heating rate within the cloud also increases with the dust-layer geometric thickness (Fig. 8b and Fig. S9). For example, the increase in heating rate ranges between ≈ 0.2 and 1.46 K day^{-1} for dust-base height at 2 km as the geometric thickness increases from 0.5 to 3.5 km.

Similar to the heating rate changes as a function of geometric thickness for the same dust-base heights,
805 there are also notable changes in the dust-induced heating rates as a function of dust-base altitudes for the same geometric thickness. For example, with dust layer geometric thickness of 2.5 km, the dust-induced longwave warming at the cloud top increases from around 0.85 K day^{-1} to around 1.25 K day^{-1} between the dust base of 1 to 3 km (see orange bars in Fig. 8b). As indicated above and regardless of the dust-
810 layer configurations, these increases in dust-induced longwave warming reduce the mean longwave cooling near the cloud top (compare Fig. 8b and Fig. 7), with a more significant reduction for thicker dust layers. Overall, our results indicate that dust-induced longwave warming accounts for an average decrease of -9.3 % (up to -18.7 % depending on dust-layer configuration) of the overall total radiative cooling near the low-level cloud top over the North Atlantic Ocean.

3.4.2 Influence of dust optical depth on dust-induced heating rates



815

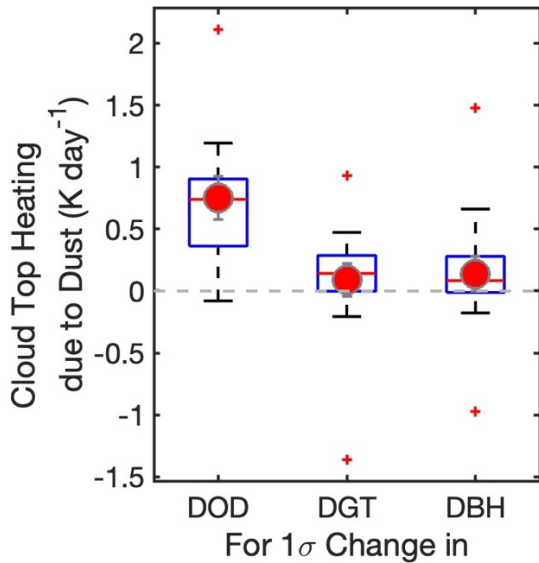
Figure 9: The total (shortwave + longwave) heating rate ($K\ day^{-1}$) within (a) the dust layer and at (b) the cloud top are categorized by dust layer base height and geometric thickness. Grey circles indicate heating rates for low dust optical depth, while black circles indicate high dust optical depth. Error bars represent the standard error. The bars represent categories with the same base height group, and those with the same geometric thickness are represented by the same colors across the different groups. The height of the bars corresponds to geometrical thickness: 0.5 km (violet), 1.5 km (light yellow), 2.5 km (orange), and 3.5 km (yellow) at the dust-layer base of 1, 2, 3, and 4 km. Dust-induced cloud-top heating response to (c) dust layer geometrical thickness ($\frac{\partial LwHt_{cldtop}}{\partial DGT}$; $K\ day^{-1} DOD^{-1} km^{-1}$), shown for categories with differing dust-layer base heights, and (d) dust base height ($\frac{\partial LwHt_{cldtop}}{\partial DBH}$; $K\ day^{-1} DOD^{-1} km^{-1}$), displayed for categories with differing geometrical thicknesses. Blue bars are for low DOD, and red bars are for high DOD. Numbers annotated with bars are percentages relative to the mean value of dust-induced cloud top heating ($3.7 \pm 0.7 K\ day^{-1} DOD^{-1}$). Mean percentage values are written in bold font.

Although the above result shows changes in radiative heating rates due to dust-layer geometric thickness for different dust-base heights, the dust-induced heating/cooling within the dust layer and at the cloud top also varies with dust optical depth. Similar to Fig. 5 above, we separated the radiative heating rates into cases of low and high DOD (Fig. 9 and Fig. S10). Within the dust layer, the all-sky total warming is 835 significantly higher for high DOD than for low DOD cases. For low DOD, the total warming in the dust layer is $4.5 \pm 1.6 \text{ K day}^{-1}$, with 20.3 K day^{-1} from shortwave warming and -15.8 K day^{-1} from longwave cooling (see Fig. 9a & S11). This total warming with the dust layer doubles (to about $9.8 \pm 3.8 \text{ K day}^{-1}$) for high DOD cases, with 29.7 K day^{-1} from the shortwave warming and -19.9 K day^{-1} from longwave cooling (Fig. 9a & S11). Essentially, shortwave warming increases faster per unit increase in dust optical 840 depth than longwave cooling (Fig. S11). Despite the significant change in dust-layer shortwave warming, the dust-induced radiative heating changes near the cloud top are controlled primarily by the longwave component, both for low and high DOD cases (Fig. 9 & S11). Near the cloud top, the overall all-sky longwave cooling does not significantly differ (Fig. S11), but the dust-induced longwave warming is more than doubled between low and high DOD cases (Fig. 9b). Specifically, the average dust-induced cloud- 845 top heating rates, dominated by dust-induced longwave warming, show values of $0.51 (\pm 0.12) \text{ K day}^{-1}$ for low DOD case and $1.34 (\pm 0.22) \text{ K day}^{-1}$ for high DOD case (Fig. 9b). Our result of dust-induced warming near cloud top is consistent regardless of DOD classification or range used (Fig. S12). As a result, we calculated the heating rate response of the dust-induced cloud-top radiative warming to a unit increase in DOD ($\frac{\partial LwHt_{cldtop}}{\partial DOD}$), and found a consistent pattern of increased dust-induced warming for all combinations 850 of dust-base height and geometrical thickness.

Regardless of DOD, dust-induced longwave warming at the cloud-top remains dependent on base height and the geometric thickness of the dust layer, as highlighted by Figure 9. To further understand the dependence of cloud-top longwave radiative heating changes on dust-layer characteristics, we estimated 855 the dust-induced longwave warming response to dust base height and the geometric thickness for low and high DOD cases, similar to the low-level cloud response (compare Fig. 9c&d to Fig. 5b & c). We find that the dust-induced DOD-normalized cloud-top longwave warming response per unit increases in geometric thickness ($\frac{\partial LwHt_{cldtop}}{\partial DGT}$) is positive for most dust base heights (Fig. 9c). In other words, for every increase in dust geometric thickness, the dust-induced longwave warming increases per unit DOD at the 860 cloud top. The only exception is for the closest dust layer to the cloud top, where there is a higher possibility of longwave cooling within the dust layer extending to the cloud top as the geometric thickness increases, and also there are higher uncertainties in estimated low-level cloud responses (cf. Fig. 5, S6, and Fig. S12). Overall, the dust-induced cloud-top longwave warming response per unit DOD to increase

geometric thickness is higher for low DOD cases, which is 13.8% of the mean dust-induced cloud top heating ($3.7 \pm 0.7 \text{ K day}^{-1} \text{ DOD}^{-1}$), than high DOD cases, which amounts to 7.1%. Similar to the geometric thickness, the dust-induced cloud-top longwave warming response per unit DOD to increases in dust-base heights ($\frac{\partial LwHt_{cltop}}{\partial DBH}$) is also generally positive, although with varying magnitude for categories of dust-layer geometric thicknesses (Fig. 9c). On average, mean dust-induced cloud-top longwave warming responses per unit DOD to increases in dust-base heights (10.3% and 10.6%) are approximately the same for low and high DOD categories (Fig. 9d).

3.4.3 Contributions of dust-layer characteristics and optical depth to dust-induced radiative warming near cloud top.



875 **Figure 10: Box-and-whisker plot showing dust-induced cloud top heating (K day^{-1}) for a 1σ (1 standard deviation) change in dust optical depth (DOD; $1\sigma = 0.27$), geometric thickness (DGT; $1\sigma = 0.964 \text{ km}$), and dust base height (DBH; $1\sigma = 0.778 \text{ km}$). Red circles represent the mean values, with error bars indicating the standard error.**

880 The results above have shown that there are general increases in dust-induced longwave warming for a unit increase in dust-layer base height and geometric thickness, as well as dust optical depth. To understand the relative impacts of these parameters on the dust-induced cloud-top longwave warming response, we estimate the dust-induced cloud-top heating one per standard deviation change in each variable ($\sigma_X \frac{\partial LwHt_{cltop}}{\partial X}$; where X is DOD, DGT or DBH and σ_X is their standard deviations; compare Fig. 885 10 and Fig. 6). While one standard deviation increases in dust-layer geometric thickness or base height

result in increases in dust-induced longwave warming at cloud top, their contributions are smaller than those due to dust optical depth. The contributions of dust optical depth to cloud top dust-induced longwave warming are about 8 times larger compared to the contribution due to dust geometric thickness, and about 6 times larger compared to the contribution due to dust base height. Specifically, dust-induced cloud-top heating increases by $0.75 (\pm 0.17)$ K day $^{-1}$ for a one-standard-deviation increase in dust optical depth, while it increases by $0.09 (\pm 0.13)$ K day $^{-1}$ and $0.13 (\pm 0.14)$ K day $^{-1}$ per one-standard-deviation increase in dust geometric thickness and dust-base height, respectively (see Fig. 10).

3.4.4 Sensitivity to cloud-top longwave warming to dust absorption properties

While the contribution of dust optical depth to the dust-induced cloud-top longwave warming response is stronger than the contribution of other dust-layer characteristics (e.g., Fig. 10), the impact of dust optical depth sensitivity depends on dust physicochemical and absorption properties, including the dust size distribution and dust complex refractive indices. Because the same dust optical depth can be achieved for different combinations of dust size distribution and refractive index, accurate representation of these properties becomes important to estimate dust-induced cloud-top longwave warming and its influence on low-level cloudiness. In addition, because these dust properties are difficult to measure from remote sensing and our current understanding mostly relies on limited in-situ measurements, dust models used in radiative transfer retrievals (for example in CloudSat-CALIPSO radiative flux dataset) with limited representation of dust properties, such as using spatiotemporally invariant dust properties, are subject to large uncertainties that may bias our understanding of dust-cloud relationship. Therefore, to understand how uncertainties in dust size distribution and refractive indices may influence retrieved heating rates and dust-induced cloud-top warming, we use the SBDART model (see Section 2.2.4) with a range of observed dust properties over the North Atlantic. Essentially, the radiative transfer simulations seek to recreate the CloudSat-CALIPSO heating rates as closely as possible by using the retrieved dust properties (such as DOD and extinction profiles) and cloud properties, as well as the thermodynamic profiles (Fig. S14) provided in the same datasets, but vary the dust size distribution and complex refractive index (Fig. S4). Specifically, we consider three measurement-based particle size distributions representing dust at source regions (volume mean diameter, D_{vm} $18.02 \mu\text{m}$), mid-range transport ($16.86 \mu\text{m}$), and after long-range transport ($3.36 \mu\text{m}$) (Fig. S13a). The coarse-mode fraction decreases from around 89% near the source to approximately 50% for long-range transport. In addition, we use three different measurements of refractive indices, including from Di Biagio et al. (2019), Optical Properties of Aerosols and Clouds (OPAC, Hess et al., 1998), and Volz (1972), with shortwave imaginary values of 0.0026, 0.0075, and 0.0080 at $0.5 \mu\text{m}$ (see Fig S4c) and longwave imaginary refractive indices at $10 \mu\text{m}$, 0.3534, 0.4783, and 0.1620 respectively. These combinations yield nine cases with spectrally varying extinction efficiency, single-scattering albedo, and asymmetry parameters, which serve as inputs to SBDART to examine the sensitivity of dust-induced heating to changes in size and absorption properties, to understand how the

unaccounted uncertainties in the dust absorption spectrum may affect dust-induced cloud-top warming (see Fig. S4 e-f).

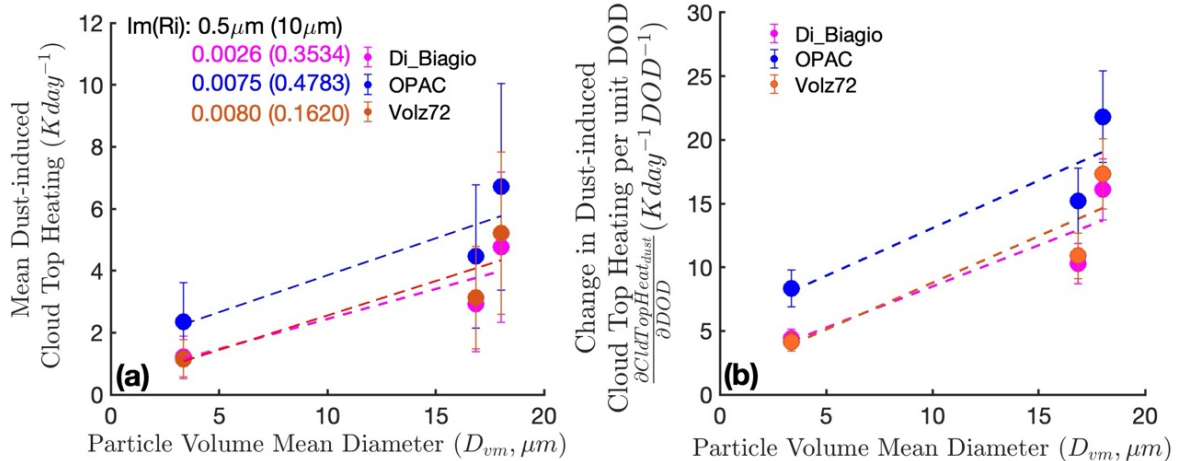


Figure 11: (a) Mean cloud top heating due to dust ($CldTopHeat_{dust}$) and (b) its sensitivity to dust optical depth ($\frac{\partial CldTopHeat_{dust}}{\partial DOD}$; $K \text{ day}^{-1} \text{ DOD}^{-1}$) for different dust particle volume diameter and refractive index. The x-axis shows the particle volume mean diameter (D_{vm} , μm). Colors indicate refractive index sources: Di_Biagio (magenta), OPAC (Blue), and Volz72 (orange). Corresponding imaginary parts of refractive indices are shown $\text{Im}(\text{Ri})$ for wavelengths $0.5\mu\text{m}$ (and $10\mu\text{m}$). Error bars denote standard deviation.

925

930

935

940

The result shows that the cloud-top heating response to dust optical depth depends sensitively on dust size distribution and refractive indices (see Fig. 11). Specifically, near the dust source where the fraction of coarser dust particles is higher than after mid or long-range transport, the absorption of longwave radiation by these coarser particles results in stronger longwave cooling in the dust layer and thereby, a stronger dust-induced longwave warming at the low-level cloud top (Fig. 11a & Fig. S15). Between when the dust is emitted at the source and when they are transported, the fraction of coarse dust particles changes significantly, resulting in the dust-induced cloud-top heating significantly reducing along the dust transport pathway. Specifically, we find that cloud-top heating is roughly twice as strong for mid-range dust size distributions and nearly four times stronger for near-source dust size distributions, compared to those dominated by finer particles after long-range transport. For example, using refractive indices from Di Biagio, the corresponding dust-induced cloud-top heating rates are 4.76 ± 2.42 , 2.93 ± 1.54 , and 1.22 ± 0.66 K day^{-1} , for source, mid- and long-range transport, respectively (Fig. 12a), while the associated sensitivities per unit change in dust optical depth are 16.10 ± 2.39 , 10.29 ± 1.58 , and 4.4 ± 0.75 $\text{K day}^{-1} \text{ DOD}^{-1}$, respectively (Fig. 11b).

Similarly, dust layers with higher values of the imaginary part of long-wave refractive indices (at 10 μm wavelength) have stronger longwave cooling in the dust layer and stronger dust-induced longwave warming at cloud top, along with greater sensitivity per unit change in dust optical depth (see blue circles in Fig. 11a & 11b and blue bars in Fig. S15e). It is evident that while the dust heating rates depend on the spectral variation of the refractive index, the dust-induced changes in the low-level cloud top are primarily controlled by the longwave part of the spectrum. In other words, stronger longwave absorption (represented at 10 μm) than shortwave absorption (represented at 0.5 μm) dominates the dust-induced changes at cloud top. For example, simulations using the long-range dust size distribution show the strongest cloud-top warming with OPAC ($2.35 \pm 1.26 \text{ K day}^{-1}$), even though Volz72 has the highest value of shortwave imaginary refractive index at 0.5 μm wavelength (0.0080) (followed by OPAC, 0.0075, and Di Biagio, 0.0026). In contrast, OPAC has higher imaginary refractive index of 0.4783 at 10 μm wavelength compared to Di Biagio and Volz72, with 0.3534 and 0.1620, respectively, thus producing weaker cloud-top warming ($1.22 \pm 0.66 \text{ K day}^{-1}$ and $1.15 \pm 0.63 \text{ K day}^{-1}$) (see Fig. 11a). Overall, our results indicate that dust-induced longwave warming at the cloud-top is sensitive to dust absorption properties, particularly the longwave imaginary refractive index and the fraction of coarse-mode particles, which may not be accurately captured in the CloudSat-CALIPSO merged dataset that used spatially invariant dust absorption properties in the retrieval radiative fluxes.

960 3.4.5 Relationship between dust-induced longwave warming and low-level cloud response

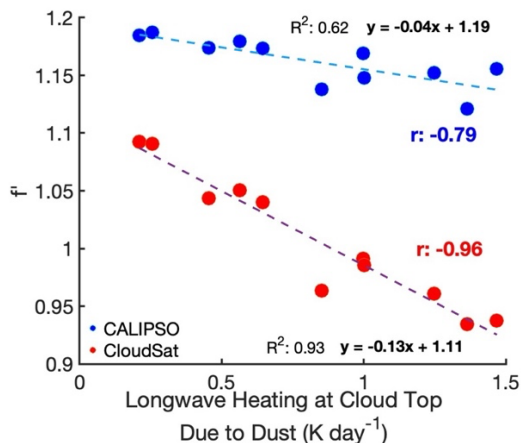


Figure 12: Scatter plot showing changes in grid-normalized cloud fraction relative to dust-induced cloud top heating. Blue circles are when cloud fraction data is used from CALIPSO, while red dots are when cloud cover is used from CloudSat.

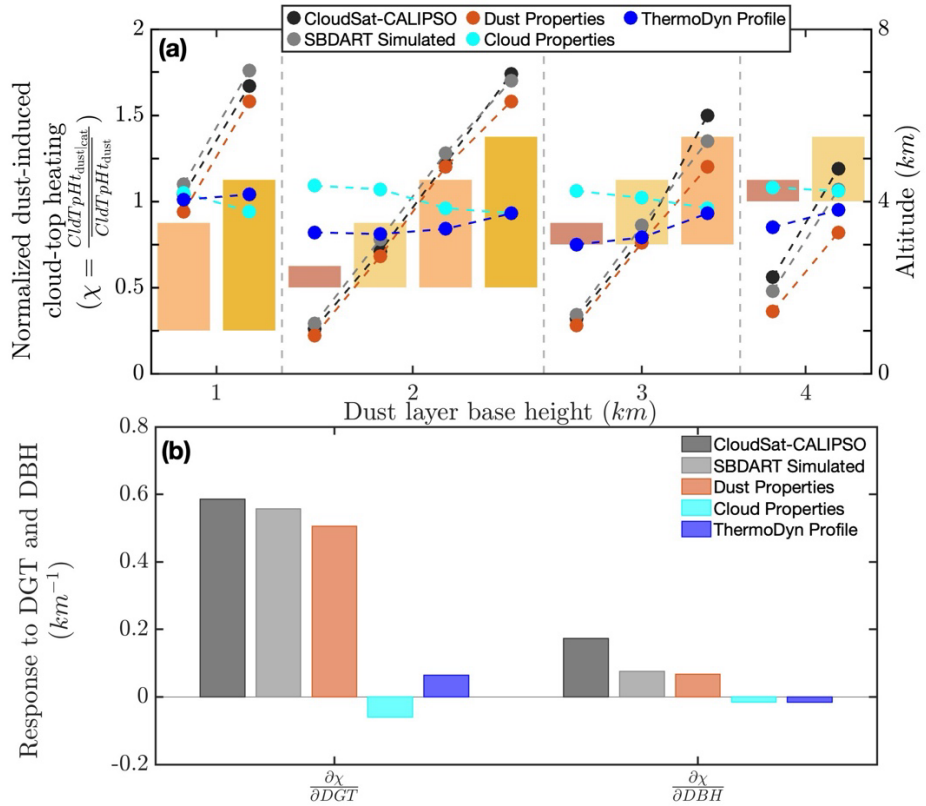
970 Despite the sensitivity to dust absorption properties, our results have shown that the dust-induced cloud-top longwave warming responses to increases in dust optical depth, dust-base height, and geometric thickness are generally consistent with similar responses of cloud fraction anomalies, although with different signs. Consequently, we find that decreases in grid-normalized cloud fraction anomalies correlate well with increases in low-level dust-induced radiative warming near the cloud top (Fig. 12).
975 Specifically, this correlation between reduced cloud fraction and increased dust-induced longwave warming is about -0.96 for CloudSat and about -0.79 for CALIPSO. This suggests that dust-included longwave warming at cloud top, which reduced the overall all-sky cloud-top longwave cooling, is primarily responsible for the decrease in low-level cloudiness when dust is above the cloud.

980 **3.5 Influence of Meteorology on the Cloud response to dust-layer Characteristics**

While we used a methodology that minimizes the influence of meteorology in our estimates, its influence may still confound the relationship between dust-induced cloud-top longwave warming and the low-level cloud responses to dust-layer characteristics and dust optical depth. Such influence may come from the instantaneous assessment of the radiative heating rates since that depends on the background 985 thermodynamic profile and/or the large-scale cloud-controlling environmental parameters, such as sea surface temperature and surface wind speed. We assess these influences on our results in the subsections below.

3.5.1 Sensitivity of dust-induced cloud-top radiative warming to background thermodynamics.

We use SBDART to separate the influence of the background thermodynamic profile, including the 990 influence of temperature and humidity, from the influence of dust properties, and examine their contribution to the simulated radiative heating rates. Like above, we do so by recreating the CloudSat-CALIPSO- heating rates as closely as possible, using the derived dust properties (such as DOD and extinction profiles) and cloud properties (such as cloud optical depth and cloud top heights), as well as the thermodynamical profiles (temperature and humidity) provided in the same datasets (see Section 2.2.4 995 for details). The variations in the simulated dust-induced shortwave and longwave heating rates for each dust-layer category are similar, although with different magnitudes (because we use different size distributions and refractive indices), as those obtained from the CloudSat-CALIPSO dataset (compare Fig. S9 and S13). Overall, the SBDART-simulated mean dust-induced cloud-top heating of 1.38 K day^{-1} (calculated using dust optical depth, extinction profiles, cloud properties, thermodynamic profiles, and a 1000 long-range transported dust size distribution with Di Biagio refractive indices) is approximately 1.7 times higher than the value estimated from CloudSat-CALIPSO data, which is 0.81 K day^{-1} . To enable comparison, both SBDART-simulated and CloudSat-CALIPSO-derived heating values across categories were normalized by their respective means (see Fig. 13a; compare black circles with grey circles).



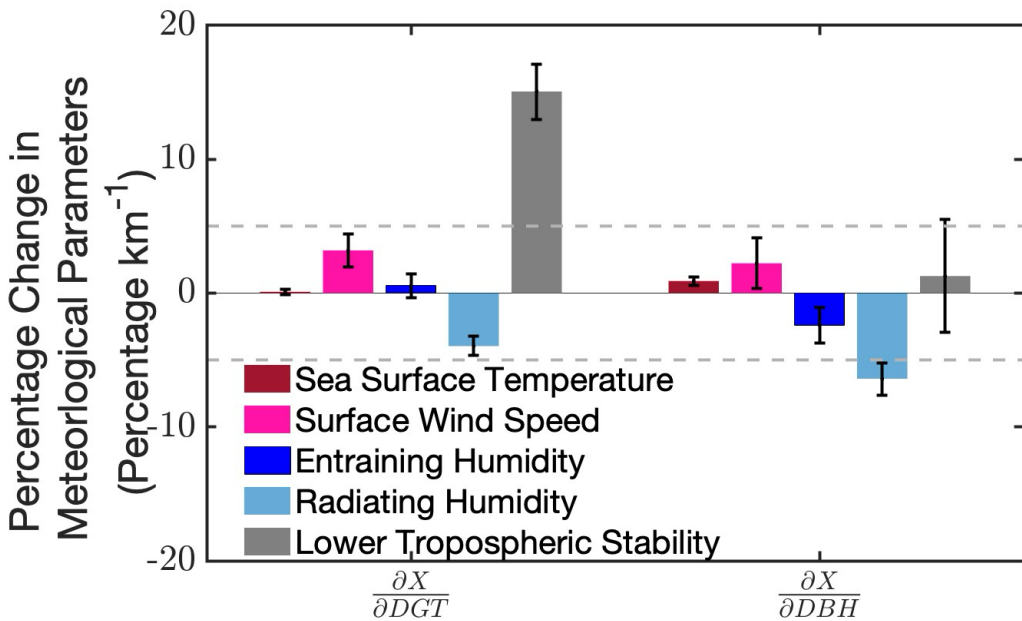
1005 **Figure 13:(a)** Normalized dust-induced cloud-top heating across dust-layer categories ($\chi = \frac{CldTpHt_{dust}|_{cat}}{CldTpHt_{dust}}$). Cloud-top heating derived from the CloudSat-CALIPSO dataset (black markers) is
 normalized by mean across categories (0.81 K day^{-1}), while SBDART-simulated heating (grey, orange, cyan, blue markers) is normalized by the corresponding simulated mean across categories
 (1.38 K day^{-1}). Grey markers show simulations with all factors varying. Orange, cyan, and blue
 markers isolate the effects of dust properties, cloud properties, and thermodynamic profiles,
 respectively. Bars show the dust categories, with the right y-axis as altitude (b) Cloud-top heating
 response to a 1 km increase in dust layer thickness and base altitude. Black bars represent
 sensitivities derived from CloudSat-CALIPSO. Grey bars show the total SBDART-simulated
 response with all factors varying. Orange, cyan, and blue bars isolate the effects of dust properties,
 cloud properties, and thermodynamic profiles, respectively.

Consequently, we estimated the sensitivity of the dust-induced cloud-top warming to variabilities in dust properties, cloud properties, and thermodynamic profiles by differencing with the simulation that replaces each set of parameters with their mean state (see Fig. S14 and Table S1). Therefore, with these 1020 simulations, we can estimate the contributions of the variabilities in each parameter to the simulated dust-induced cloud-top heating (see Section 2.2.4 for details). The result shows that the response of the cloud-

top heating rate to dust-layer characteristics is less sensitive to the variabilities in the cloud properties and background thermodynamic profiles, thereby contributing less to the overall dust-induced cloud-top heating rate when compared to the variabilities in dust properties (Fig. 13b). The influence is despite the co-variabilities in the cloud properties and thermodynamic profiles with the dust-layer properties, including dust-layer geometric thickness and dust-base height (e.g., Fig. S14). The responses of the normalized dust-induced cloud-top heating to a unit increase in dust-layer geometric thickness are 0.51 km^{-1} when only dust properties are varied (orange bars in Fig. 13b), 0.06 km^{-1} when only thermodynamic profiles are varied (blue bars in Fig. 13b), and -0.06 km^{-1} when only cloud properties are varied (cyan bars in Fig. 13b). Similarly, the responses of the normalized dust-induced cloud-top heating to a unit increase in dust-layer base height are 0.07 km^{-1} when only dust properties are varied, -0.02 km^{-1} when only thermodynamic profiles or cloud properties are varied. The lower sensitivity to the thermodynamic profile may partly result from the limited influence of moisture, despite higher relative humidity within the dust layer (see Fig. 2c and Fig. S14), as dust particles are largely non-hygroscopic, meaning their size and optical depth do not substantially increase with humidity. This highlights the dominant role of dust properties in the estimated dust-induced cloud-top heating, and consequently, its relationship to the reduced cloud fraction when dust is above the cloud. Overall, our results show that dust-induced cloud-top radiative warming is more sensitive to changes in dust properties, contributing more than 90% of the estimated dust-induced cloud-top warming, than to changes in cloud properties or thermodynamic profiles.

3.5.2 Influence of Other Meteorological Variables on cloud response to dust-layer characteristics

In addition to examining the sensitivity of our results to the variabilities in cloud properties and thermodynamic profiles represented by the background temperature and moisture profiles, we also examined the influence of other cloud-controlling parameters that may be linked to large-scale atmospheric conditions. We focus on cloud-controlling parameters that have been identified by previous studies over the North Atlantic region, including sea surface temperature (SST), wind speed, lower tropospheric stability, and above-cloud humidity (Klein et al., 2017; Naud et al., 2023). To minimize the influence of these cloud-controlling factors, we confined our analysis to $5^\circ \times 5^\circ$ grid boxes, where we assume the meteorological variability is small when focused on a single season for a long-term period. While our approach is designed to minimize the overall influence of meteorology and reduce the impact of possible co-variability between meteorological conditions and aerosols on the low-level cloud cover, we further examine how the other well-known cloud-controlling factors may change for each category used in our analysis (e.g., Fig. 4).



1055 **Figure 14: Percentage change in key meteorological variables per kilometer increase in dust layer
geometrical thickness and base height. Shown variables include sea surface temperature (SST, red),
surface wind speed (magenta), entraining humidity (dark blue), radiating humidity (light blue),
and lower tropospheric stability (LTS, grey). Percentage changes are computed relative to the
domain-mean values of each variable: SST = 25°C, wind speed = 6.04 m s⁻¹, entraining humidity =
1060 0.0077 kg/kg, radiating humidity = 0.0066 kg/kg, and LTS = 7.08°C. Error bars are the standard
error for respective parameters. Grey dotted horizontal lines are 5% lines.**

We find minimal variation in most cloud-controlling factors across our defined categories (Fig. S16), and their weak sensitivity to changes in dust geometric thickness and dust base height (Fig. 14) suggests
1065 limited influence of these factors on the estimated cloud response to dust-layer characteristics. Like
percentage cloud response (Fig. 4b &c) and cloud top heating response (Fig. 9b&c) to per one-kilometer
increase in DGT and DBH, we estimated percentage changes for relevant meteorological parameters to
DGT and DBH changes (see Fig. 14). Most of the meteorological variables that can affect the cloud cover
1070 show less than 5% changes to increase in DGT and DBH. For example, a kilometer increase in DGT is
associated with only a 0.54% increase in SST (red bars in Fig. 14) and a 3.1% increase in surface wind
speed (magenta bars in Fig. 14). In the case of DBH, these changes are, 0.9% for SST and 2.2 % for
windspeed (see red and magenta bars in Fig 14). Similarly, the above-cloud moisture has minimal impacts
on the low-level cloud response to dust-layer characteristics. As shown in Fig. 13, meteorological impacts
1075 on the response of cloud-top dust-induced longwave warming to dust-layer characteristics were small
despite the mid-tropospheric high relative humidity used in the radiative transfer simulations (see also
Fig. S16). To show further the minimal impacts of above-cloud moisture in our analysis, we estimated

two grid-scale humidity measures following Eastman and Wood (2018): entraining humidity (adjacent to the cloud top) and radiating humidity (the average humidity between 700 hPa and the entraining layer, as discussed in Section 2.2.6). Radiating humidity emits downwelling longwave radiation, affecting cloud-top cooling (Yamaguchi et al., 2015), while higher entraining humidity reduces droplet evaporation, lowering the likelihood of cloud breakup. We find both entraining and radiating humidity anomalies change very little across categories (see Fig. S16c & S16d), similar to changes in SST and wind speed anomalies. Specifically, the changes in entraining and radiating humidities per one-kilometer increase of DGT are about 3% and for DBH it is below 6 % of the domain mean values, respectively (see blue bars in Fig. 14). Overall, the changes in sea surface temperature, surface winds, and above-cloud moisture cannot explain the large changes in low-level cloud response to unit increase in dust-layer characteristics and properties.

In contrast to wind speed, SST, and above-cloud moisture anomalies, the change in LTS is substantial across the dust categories (Fig. S16e). Specifically, we find that for per kilometer increase in DGT, LTS anomalies increase by 15% (first grey bar in Fig. 14), while for DBH increase, LTS change is 1.27% (second grey bar in Fig. 14). This result is consistent with previous studies of dust above clouds, where increases in LTS attributed to shortwave warming in the dust layer have been associated with increases in low-level cloudiness (Doherty and Evan, 2014). This relationship between LTS and enhancement of low-level cloud cover was often explained by boundary-layer moisture build-up, resulting in increases in cloud-top longwave cooling and consequently increases in cloud fraction (e.g., Wilcox et al., 2009). However, our results show an observed reduction in low-level cloud fraction associated with increasing dust-induced cloud-top warming when the dust-layer geometric thickness and optical properties are increased. Our results further suggest that dust-induced longwave warming at the cloud top may offset the influence of LTS on the mean cloud-top cooling, and, while LTS may be important for low-level cloud enhancement and dust semi-direct effect, the influence of LTS may only be stronger in low dust conditions, with less coarse dust particles and less overall longwave absorption.

4. Discussion and Summary

We have shown that low-level cloud response is sensitive to the dust-layer altitude, geometric thickness, and dust optical depth, influencing the dust-induced longwave warming and counteracting the mean radiative cooling near the low-level cloud top. We do so by leveraging vertically-resolved aerosol, cloud, and radiative heating rates information from CALIOP and the merged CALIPSO-CloudSat products, as well as the Santa Barbara DISORT Atmospheric Radiative Transfer (SBDART) model between May and August (2007 – 2017) over the tropical North Atlantic Ocean (55W-20W; 5N-30N). During this period, when the mean low-level cloud top height is approximately 1.35 km (± 0.05 km), we showed that nearly 78% of the total dust column burden is situated above the cloud layer. We use profiles with CloudSat-

CALIPSO retrieved dust layer and single-layer low-level clouds, and require a minimum of 200 m between them to minimize potential biases that can be introduced through uncertainties in the retrieved layer information. Furthermore, we also minimize large-scale meteorological variability by dividing the broad region into a $5^\circ \times 5^\circ$ degree grid box following previous studies (Adebiyi and Zuidema, 2018; Loeb and Schuster, 2008). We categorized dust and cloud profiles within each $5^\circ \times 5^\circ$ grid box based on the dust layer base height (1, 2, 3, and 4 km) and geometrical thickness (0.5, 1.5, 2.5, and 3.5 km) only when aerosols, clouds, and radiative flux information are all available to obtain statistically robust relationships. Out of the possible 16 categories of dust-layer base height and geometric thickness, only 11 satisfy our stringent requirements of the minimum number of profiles within each category and the minimum number of total $5^\circ \times 5^\circ$ grid boxes allowed.

Whereas low-level cloudiness typically increases due to the presence of the above-cloud dust layer through the process of dust semi-direct effect (Amiri-Farahani et al., 2017), we find that the extent of such increases depends on the dust layer's optical properties as well as its altitude and geometrical thickness. Using the above dust-layer categories, our results indicate decreases in low-level cloud response, that is, the rate of change of grid-normalized low-level cloud fraction relative to basin-wide mean per increase in dust-base height, geometric thickness, and dust optical depth. Specifically, our results suggest the following: First, the low-level cloud response is strongly influenced by both the altitude of the dust layer base and its geometric thickness. On average, cloud fraction decreases by 1.7% and 5.1% for each kilometer increase in dust-layer geometric thickness based on CALIPSO and CloudSat, respectively. While the cloud response to geometric thickness consistently leads to a reduction regardless of dust base height, the grid-normalized low-level cloud response to a one-unit change in dust-base height depends on the dust-layer geometric thickness. Specifically, for thinner dust layers, one unit increase in dust-layer base height reduces cloud cover by 0.5% and 1.4% for geometric thickness values of 0.5 km and 1.5 km, respectively, using CALIPSO data and 2.3% and 3.0%, respectively, using CloudSat. In contrast, for thick dust layers (GT=3.5 km), increasing the base height leads to an increase in cloud response, with values of 3.2% and 0.3% from CALIPSO and CloudSat data, respectively.

Second, we estimate cloud response to dust optical depth and found that the mean low-level cloud fraction decreases by approximately 17% for every unit change in dust optical depth. Consequently, when we divided the dust-layer categories into low and high dust optical depth cases, the low-level cloud response to dust-layer geometric thickness is stronger for high dust optical depth, despite having lower grid-normalized cloud fraction, than for low dust optical depth cases. Specifically, for a 1 km increase in dust-layer base, the negative cloud responses change by about 0.7% (-0.1% and 0.6%, respectively) between the low and high dust optical depth categories. Similarly, for a 1 km increase in dust-layer geometric thickness, the negative cloud responses change by about 1.6% (-0.86 % and -2.49%, respectively) between the low and high dust optical depth categories. Finally, we estimate the relative contribution of the dust-

layer characteristics and dust optical depth by estimating the sensitivity in the low-level cloud response to a one-standard-deviation (1σ) increase in each parameter. We find that the negative low-level cloud response is stronger for a 1σ change in dust optical depth than for a 1σ change in dust-layer geometric thickness or dust-base heights. Specifically, we find that the relative reduction in low-level cloud response to 1σ increase in dust optical depth is about $-4.3 (\pm 1.04)\%$, compared to $-1.6 (\pm 0.65)\%$ and $0.19 (\pm 0.45)\%$ to 1σ change in dust-layer geometric thickness and dust base respectively, indicating that the changes in low-level cloud fraction due to 1σ change in dust optical depth is about three times stronger than 1σ change in geometric thickness, and significantly more than 1σ change in dust-base height that is largely negligible within the error range.

We hypothesized that the variations in radiative fluxes at the low-level cloud top drive the observed cloud responses to perturbations in dust-base heights, geometric thickness, and dust optical depth. To show this relationship, we used the CALIPSO-CloudSat combined product to estimate radiative heating rates (both shortwave and longwave) for each defined dust category. We find that the dust layers above the low-level clouds induce anomalous longwave warming near the cloud top that counteracts the mean cloud-top radiative cooling and can reduce the total cloud-top cooling by as much as 18.7% (mean of 9.3%). In addition, our results further showed that this dust-induced cloud-top longwave warming increases with an increase in dust optical depth, dust-layer geometric thickness, and dust-base height. However, a 1σ increase in dust optical depth results in a significantly stronger dust-induced cloud-top warming ($\approx 0.75 \pm 0.17 \text{ K day}^{-1}$), nearly 8 times greater than the warming from a 1σ increase in geometric thickness ($0.09 \pm 0.13 \text{ K day}^{-1}$) and 6 times greater than the warming from a 1σ increase in dust base height ($0.13 \pm 0.14 \text{ K day}^{-1}$). Consequently, we find that decreases in low-level cloud fraction response correlate well (0.79 for CALIPSO and 0.96 for CloudSat) with responses in dust-induced radiative warming near the cloud top. This suggests that dust-induced longwave warming, which reduced the overall cloud-top longwave cooling, is primarily responsible for the decrease in low-level cloudiness when above-cloud dust-layer characteristics and dust optical depth are increased.

While the contribution of dust optical depth to the dust-induced cloud-top longwave warming response is stronger than other dust-layer characteristics, our results further show that the impacts of dust optical depth on low-level clouds sensitively depend on dust absorption properties, including the dust size distribution and dust complex refractive indices. To understand how uncertainties in absorption properties may influence the estimated dust-induced cloud-top warming and consequently the low-level cloud fraction, we use the SBDART (Santa Barbara DISORT Atmospheric Radiative Transfer) model to recreate the CloudSat-CALIPSO heating rates as closely as possible by using the retrieved dust properties (such as dust optical depth and extinction profiles) and cloud properties, as well as the thermodynamic profiles provided in the same datasets, but vary the dust size distribution and complex refractive index based on previously-published measurements. The result shows that dust-induced longwave warming at

the cloud top is highly sensitive to the coarse-mode fraction of the dust size distribution and the imaginary part of the longwave refractive index. For example, near-source and mid-range-transported dust size distributions containing approximately 89% and 83% coarse-mode fraction produce nearly four and two times more warming, respectively, than one long-range-transported dust size distribution with only 50% coarse-mode fraction. Similarly, higher values of the longwave imaginary refractive index, which indicate stronger dust-layer longwave absorption, also lead to enhanced dust-induced cloud-top warming. Therefore, our result suggests that the contribution of the dust-induced cloud-top longwave warming that counteracts the mean cloud-top radiative cooling may be larger than indicated above, if the spatiotemporally varying dust size distribution and refractive index are accurately represented.

While we minimize the influence of potential meteorological co-variability in our analysis, we further assess its impact on the relationship between dust-induced cloud-top longwave warming and the low-level cloud response. First, similar to the sensitivity analysis above, we also reproduced CALIPSO-

CloudSat heating profiles using SBDART and performed sensitivity experiments by varying dust-layer properties, cloud properties (including the cloud optical depth and cloud top heights), and thermodynamic profiles (represented by the temperature and humidity profiles). The result showed that the estimated low-level cloud response when dust is above the cloud can be primarily attributed to dust-layer characteristics

and properties, which dominate changes in dust-induced reduction in cloud-top longwave cooling. Although the response of the cloud-top heating rates to dust-layer characteristics also covaries with cloud properties and the background thermodynamic profiles, specifically the changes in humidity profile above the clouds, their contributions to the overall dust-induced cloud-top heating rate are less compared to the dust properties. Second, we also examined the influence of other cloud-controlling parameters, including

sea surface temperature, wind speed, and above-cloud moisture that may be linked to large-scale atmospheric conditions. The result showed minimal and non-systematic variations in these parameters across dust categories, suggesting that they have limited or no influence on the observed instantaneous relationship between low-level cloudiness and anomalous dust-induced cloud-top longwave warming.

Although we find an increase in LTS for higher geometrically and optically thick layers, consistent with previous studies, they contradict the observed decrease in low-level cloudiness for the dust categories. Overall, our results indicate that the relationship between low-level cloudiness and dust-induced cloud-top radiative warming is more sensitive to changes in dust properties than to meteorological variabilities.

Our results have important implications for our understanding of low-level cloud response and the dust semi-direct effect over the North Atlantic Ocean. First, our result suggests that processes associated with low-level cloud response when the dust layer is above the cloud and, consequently, the dust semi-direct effect, are more sensitive to changes in cloud-top radiative cooling. Previous studies have shown the significance of cloud-top radiative cooling in driving the cloud-top turbulence, convective instability,

1220 mixing in the cloud layer, and small-scale dry air entrainment, which is important for cloud development
(Wood, 2012; Zuidema et al., 2019). A reduction in cloud-top radiative cooling could facilitate a reduction
in cloud fraction through several different pathways. One such pathway is that a reduction in cloud-top
radiative cooling may lead to weaker turbulent mixing within the cloud, potentially resulting in
1225 decoupling and stratification of the boundary layer, which limits the surface moisture source into the
cloud layer and subsequently reduces cloudiness (e.g., Bretherton and Wyant, 1997). Such pathways tend
to result in an increase in the frequency of cumulus clouds rather than stratus clouds. Another pathway is
through the entrainment of dry air at the cloud top, whereby a reduction in cloud-top radiative cooling
will result in the weakening of the entrainment interfacial layer, allowing more dry and warm air from the
free troposphere to mix into the cloud layer, thereby leading to reduced cloudiness (Wood, 2012b). For
1230 example, Wood (2012) highlighted that because a lower surface-based lifting condensation layer than the
cloud-top inversion layer is required to maintain low-level cloudiness, 1 K of warming within the cloud
layer aided by reduction of cloud-top radiative cooling or associated entrainment of dry air could lift
condensation layer much faster than it lifts the cloud-top inversion layer, hence resulting in a reduction
1235 in cloudiness. Assuming other critical environmental factors remain constant, these pathways could result
in a feedback process where a reduction in cloudiness can result in a further reduction in cloud-top
radiative cooling and a further reduction in cloudiness (Bretherton, 2015; Cessi et al., 2017). Such
feedback relationships have been used to explain the stratocumulus to cumulus transition, which also
exists over the North Atlantic Ocean (Sandu and Stevens, 2011). Our result, therefore, suggests that dust-
1240 induced longwave warming at the cloud top facilitates the reduction of low-level cloudiness, and those
changes are strongly dependent on the dust layer's height, geometric thickness, and optical depth as well
as dust absorption properties, including dust size distribution and refractive index.

Second, our result of radiative changes and cloud responses to the above-cloud dust layer adds to the
1245 traditional process associated with cloud responses to other above-cloud absorbing aerosols, such as
biomass-burning smoke aerosols above low-level clouds of the southeast Atlantic Ocean. Our results
highlight that, in addition to the shortwave absorption that has been traditionally associated with low-
level cloudiness and its aerosol semi-direct effect, the longwave effect could also play a substantial role.
Specifically, the shortwave warming by the dust layer likely increases the lower-tropospheric stability for
1250 optically and geometrically thicker dust layers, similar to smoke aerosols, where such increased stability
would enhance low-level cloudiness (e.g., Wilcox, 2010, 2012). However, unlike smoke aerosols, the
dust-induced longwave warming that reduces the mean cloud-top radiative cooling can affect cloud
development and reduce low-level cloudiness, similar to the radiative effects of above-cloud moisture,
carbon dioxide, and free-tropospheric clouds on low-level clouds, as shown by previous studies(Adebiyi
1255 et al., 2015; Adebiyi and Zuidema, 2018; Christensen et al., 2013; Singer and Schneider, 2023). This
interplay between shortwave and longwave effects on the clouds defines the dust semi-direct effect, where
cloud responses play a pivotal role in deciding whether the overall effect will be dominated by the

radiative warming (positive SDE) or cooling (negative SDE) at the top of the atmosphere. Specifically, the stability effect induced by the shortwave warming within the dust layer tends to increase low-level cloudiness, resulting in negative dust SDE, but counteracted by the dust-induced longwave warming that reduces the cloud-top cooling and may suppress the stability effects of shortwave absorption, therefore, leading to reduction the low-level cloudiness and tipping the balance toward positive dust SDE. The total dust SDE, therefore, emerges as the outcome of competing longwave and shortwave effects. Our analysis shows that the relative contributions of these effects depend on the vertical positioning of the dust layer relative to the cloud and the layer's optical and geometrical properties.

1265

We note some caveats in our analysis. First, our study relies on instantaneous snapshots from CALIPSO-CloudSat profiles, which do not capture the full temporal dynamics, including diurnal variation, of the low-level clouds over the region. In addition, while these profiles provide vertical distributions of clouds and aerosols—suitable for our analysis and useful to compare with snapshots from passive sensors like 1270 MODIS—the CALIOP sensors have limited capability in detecting aerosols below clouds (Yu et al., 2015). As a result, the selected profiles for the above-cloud dust cases might not be entirely free from the influence of aerosols below the cloud. This limitation introduces uncertainty, as aerosols below the cloud could affect cloud cover by altering cloud microphysics and, subsequently, the overall cloud response. 1275 Such aerosols may influence processes like droplet formation, cloud lifetime, and cloud cover, thereby complicating the interpretation of our results. However, this uncertainty cannot be addressed using the datasets and methodology employed in this study, and further research using numerical models may be required to accurately quantify these effects. Second, although we found minimal and non-systematic variation across the categories in meteorological cloud-controlling factors, highlighting their non-significant effect on our analysis, their role cannot be fully quantified. Specifically, the dust layer over 1280 the North Atlantic, similar to smoke over the South Atlantic, has been found to contain relatively higher moisture content (Ryder, 2021). Thus, the uncertainty related to above-cloud humidity remains a critical factor, although we attempt to account for this by using the radiating and entraining humidity parameters (Fig. 12).

1285

In addition to these caveats, limitations in our methodological approach may also introduce possible uncertainties in our estimates. First, while we chose only profiles having a minimum separation of 200 m between the cloud top and the dust-layer base to account for retrieval biases and avoid any microphysical interactions (see Section 2.2.1), variabilities in the dust-layer base may result in associated variations in cloud-top height that may confound with the radiative impact of the dust layer. Specifically, when the 1290 dust base is low (e.g., 1 km), only profiles having clouds with very low top heights were allowed, while profiles having higher dust-layer base height can allow clouds with higher cloud tops. As a result, the observed cloud response to dust base height could be influenced by variations in cloud-top height across these categories. However, aside from the 1 km dust base category, cloud-top heights across other dust

base height groups are broadly similar (see Table S1 and Fig S13), suggesting that differences in cloud
1295 top height are unlikely to significantly affect the results. In addition, the sensitivity analysis confirms that variations in cloud properties across the categories have minimal influence on the impact of dust geometric thickness and dust base height on dust-induced cloud-top heating (see Fig. 13 b and relevant discussion in Section 3.5.1). Second, while we chose defined categories for dust geometric thickness, the variabilities in dust vertical distribution within each category may have influenced the associated radiative
1300 impacts on the low-level clouds. Specifically, despite a colder dust layer top, variabilities in the vertical distribution of coarse dust may have resulted in larger dust-induced longwave warming at cloud-top for thicker than thinner dust layers. For example, for the same dust-layer base height, maximum dust longwave extinction (unlike shortwave extinction) appears skewed to the bottom of a thicker dust layer than a thinner dust layer (e.g., Fig. S9 and S13), resulting in larger downwelling longwave radiation. With
1305 the inherent correlation between dust geometric thickness and dust optical depth (e.g., Fig. S17), it is difficult to separate the resulting influence of co-variability in coarse dust vertical distribution, dust optical depth, and dust geometric thickness on the low-level cloud responses.

Despite these limitations, our result underscores the need for accurate estimates of the dust layer's vertical
1310 distribution and dust absorption properties, including dust size distribution and mineralogical composition, to accurately quantify dust SDE. Unlike above-cloud smoke, where shortwave radiative effects often suffice to explain the SDE, dust requires consideration of both shortwave and longwave influences (Baró Pérez et al., 2021; Deaconu et al., 2019; Wilcox, 2010, 2012). The longwave effect, in particular, depends on dust vertical profiles, the thickness of the dust layer, and their altitude relative to
1315 the clouds, along with particle size distributions and absorption properties. Current climate models do not accurately incorporate these parameters, leading to uncertainties in the estimation of dust's SDE (Cappa et al., 2016). Most importantly, studies have found an underestimation of large dust particles by current climate models, which may lead to potential underestimation of the longwave effect (Adebiyi et al., 2023; Adebiyi and Kok, 2020). Our study highlights the need for improved observation of global three-
1320 dimensional dust distributions, along with accurate estimations of radiatively sensitive aerosol properties, such as particle size distribution and mineralogical composition.

Data availability. Cloud and aerosol layer data used in this study were obtained from the CALIPSO Level 2 data products, including the 5 km aerosol profile product
1325 (https://doi.org/10.5067/CALIOP/CALIPSO/LID_L2_05KMAPRO-STANDARD-V4-20) and the 5 km merged layer product (https://doi.org/10.5067/CALIOP/CALIPSO/LID_L2_05KMMLAY-STANDARD-V4-20). CloudSat-CALIPSO radiative flux data were accessed from the 2B-FLXHR-LIDAR product (<https://www.cloudsat.cira.colostate.edu/data-products/2b-flxhr-lidar>). All data supporting the findings of this study are available at Zenodo: <https://doi.org/10.5281/zenodo.15571618>.

1330

Supplement. Attached is a supplement document containing additional figures and a table.

Author Contributions. AAA and SKP designed the study. SKP performed the analysis. SKP and AAA

1335 interpreted the results and wrote the paper.

Competing Interests. The contact author declared that none of the authors has any competing interests.

Acknowledgement. This study was supported by the U.S. Department of Energy (DOE), Office of

1340 Science (award #DE-SC0024281). CALIPSO data used in this study were obtained from the NASA Langley Research Center Atmospheric Science Data Center

(<https://asdc.larc.nasa.gov/project/CALIPSO>), and we acknowledge the CALIPSO science team for providing these data. CloudSat-CALIPSO radiative flux data were provided by the CloudSat Data Processing Center at Colorado State University (<https://www.cloudsat.cira.colostate.edu/>), and we thank

1345 the CloudSat team for their data processing and dissemination efforts. We acknowledge the use of the SBDART radiative transfer model, developed at the University of California, Santa Barbara, and made publicly available at <https://github.com/paulricchiazzi/SBDART>.

References

1350 Adebiyi, A. A. and Kok, J. F.: Climate models miss most of the coarse dust in the atmosphere, *Sci Adv*, 6, 1–10, <https://doi.org/10.1126/sciadv.aaz9507>, 2020.

Adebiyi, A. A., Pandey, S. K., Di Biagio, C., Chang, I., Formenti, P., and Akinsanola, A. A.: Aerosols over Africa: sources, properties, and distribution, in: *Aerosols and Precipitation Over Africa*, Elsevier, 1–64, <https://doi.org/10.1016/B978-0-44-314050-1.00006-2>, 2025.

1355 Adebiyi, A. A. and Zuidema, P.: Low cloud cover sensitivity to biomass-burning aerosols and meteorology over the Southeast Atlantic, *J Clim*, 31, 4329–4346, <https://doi.org/10.1175/JCLI-D-17-0406.1>, 2018.

Adebiyi, A. A., Zuidema, P., and Abel, S. J.: The convolution of dynamics and moisture with the presence of shortwave absorbing aerosols over the southeast Atlantic, *J Clim*, 28, 1997–2024, <https://doi.org/10.1175/JCLI-D-14-00352.1>, 2015.

1360 Adebiyi, A. A., Kok, J. F., Murray, B. J., Ryder, C. L., Stuut, J. B. W., Kahn, R. A., Knippertz, P., Formenti, P., Mahowald, N. M., Pérez García-Pando, C., Klose, M., Ansmann, A., Samset, B. H., Ito, A., Balkanski, Y., Di Biagio, C., Romanias, M. N., Huang, Y., and Meng, J.: A review of coarse mineral dust in the Earth system, *Aeolian Res*, 60, <https://doi.org/10.1016/j.aeolia.2022.100849>, 2023.

Albrecht, B. A.: Aerosols, Cloud Microphysics, and Fractional Cloudiness, *Science* (1979), 245, 1227–1230, <https://doi.org/10.1126/science.245.4923.1227>, 1989.

1365 Allen, R. J., Amiri-Farahani, A., Lamarque, J. F., Smith, C., Shindell, D., Hassan, T., and Chung, C. E.: Observationally constrained aerosol–cloud semi-direct effects, *NPJ Clim Atmos Sci*, 2, 1–12, <https://doi.org/10.1038/s41612-019-0073-9>, 2019.

1370 Amiri-Farahani, A., Allen, J. R., Neubauer, D., and Lohmann, U.: Impact of Saharan dust on North Atlantic marine stratocumulus clouds: Importance of the semidirect effect, *Atmos Chem Phys*, 17, 6305–6322, <https://doi.org/10.5194/acp-17-6305-2017>, 2017.

1375 Arola, A., Lipponen, A., Kolmonen, P., Virtanen, T. H., Bellouin, N., Grosvenor, D. P., Gryspeerdt, E., Quaas, J., and Kokkola, H.: Aerosol effects on clouds are concealed by natural cloud heterogeneity and satellite retrieval errors, *Nat Commun*, 13, 7357, <https://doi.org/10.1038/s41467-022-34948-5>, 2022.

1380 Atwater, M. A.: Planetary Albedo Changes Due to Aerosols, *Science* (1979), 170, 64–66, <https://doi.org/10.1126/science.170.3953.64>, 1970.

Baró Pérez, A., Devasthale, A., Bender, F. A. M., and Ekman, A. M. L.: Impact of smoke and non-smoke aerosols on radiation and low-level clouds over the southeast Atlantic from co-located satellite observations, *Atmos Chem Phys*, 21, 6053–6077, <https://doi.org/10.5194/acp-21-6053-2021>, 2021.

Bellouin, N.: Aerosols: Role in Climate Change, Second Edi., Elsevier, 76–85 pp., <https://doi.org/10.1016/B978-0-12-382225-3.00054-2>, 2015.

1385 Bellouin, N., Quaas, J., Gryspeerdt, E., Kinne, S., Stier, P., Watson-Parris, D., Boucher, O., Carslaw, K. S., Christensen, M., Daniau, A. -L., Dufresne, J. -L., Feingold, G., Fiedler, S., Forster, P., Gettelman, A., Haywood, J. M., Lohmann, U., Malavelle, F., Mauritzen, T., McCoy, D. T., Myhre, G., Mülmenstädt, J., Neubauer, D., Possner, A., Rugenstein, M., Sato, Y., Schulz, M., Schwartz, S. E., Sourdeval, O., Storelvmo, T., Toll, V., Winker, D., and Stevens, B.: Bounding Global Aerosol Radiative Forcing of Climate Change, *Reviews of Geophysics*, 58, 1–45, <https://doi.org/10.1029/2019RG000660>, 2020.

Bender, F. A. -M.: Aerosol Forcing: Still Uncertain, Still Relevant, *AGU Advances*, 1, <https://doi.org/10.1029/2019AV000128>, 2020.

1390 Bertrand, L., Kay, J. E., Haynes, J., and de Boer, G.: A global gridded dataset for cloud vertical structure from combined CloudSat and CALIPSO observations, *Earth Syst Sci Data*, 16, 1301–1316, <https://doi.org/10.5194/essd-16-1301-2024>, 2024.

1395 Di Biagio, C., Formenti, P., Balkanski, Y., Caponi, L., Cazaunau, M., Pangui, E., Journet, E., Nowak, S., Andreae, M. O., Kandler, K., Saeed, T., Piketh, S., Seibert, D., Williams, E., and Doussin, J.-F.: Complex refractive indices and single scattering albedo of global dust aerosols in the shortwave spectrum and relationship to iron content and size, *Atmos Chem Phys*, 19, 15503–15531, <https://doi.org/10.5194/acp-2019-145>, 2019.

Bond, T. C., Doherty, S. J., Fahey, D. W., Forster, P. M., Berntsen, T., DeAngelo, B. J., Flanner, M. G., Ghan, S., Kärcher, B., Koch, D., Kinne, S., Kondo, Y., Quinn, P. K., Sarofim, M. C., Schultz, M. G., Schulz, M., Venkataraman, C., Zhang, H., Zhang, S., Bellouin, N., Guttikunda, S. K., Hopke, P. K., Jacobson, M. Z., Kaiser, J. W., Klimont, Z., Lohmann, U.,

1400 Schwarz, J. P., Shindell, D., Storelvmo, T., Warren, S. G., and Zender, C. S.: Bounding the role of black carbon in the climate system: A scientific assessment, *Journal of Geophysical Research: Atmospheres*, 118, 5380–5552, <https://doi.org/10.1002/jgrd.50171>, 2013.

Bretherton, C. S.: Insights into low-latitude cloud feedbacks from high-resolution models, *Philosophical Transactions of the Royal Society A: Mathematical, Physical and Engineering Sciences*, 373, 20140415, <https://doi.org/10.1098/rsta.2014.0415>, 2015.

1405 Bretherton, C. S. and Wyant, M. C.: Moisture Transport, Lower-Tropospheric Stability, and Decoupling of Cloud-Topped Boundary Layers, *J Atmos Sci*, 54, 148–167, [https://doi.org/10.1175/1520-0469\(1997\)054<0148:MTLTSA>2.0.CO;2](https://doi.org/10.1175/1520-0469(1997)054<0148:MTLTSA>2.0.CO;2), 1997.

Candlish, L. M., Raddatz, R. L., Gunn, G. G., Asplin, M. G., and Barber, D. G.: A validation of cloudsat and CALIPSO's temperature, humidity, cloud detection, and cloud base height over the arctic marine cryosphere, *Atmosphere - Ocean*, 51, 1410 249–264, <https://doi.org/10.1080/07055900.2013.798582>, 2013.

Cappa, C., Kotamarthi, R., Selacek, A., Flynn, C., Lewis, E., McComiskey, A., and Riemer, N.: Absorbing Aerosols Workshop Report, January 20–21, 2016, 1–23 pp., <https://doi.org/10.2172/1471231>, 2016.

Ceppi, P., Brient, F., Zelinka, M. D., and Hartmann, D. L.: Cloud feedback mechanisms and their representation in global climate models, <https://doi.org/10.1002/wcc.465>, 2017.

1415 Chen, B., Huang, J., Minnis, P., Hu, Y., Yi, Y., Liu, Z., Zhang, D., and Wang, X.: Detection of dust aerosol by combining CALIPSO active lidar and passive IIR measurements, *Atmos Chem Phys*, 10, 4241–4251, <https://doi.org/10.5194/acp-10-4241-2010>, 2010.

Chlek, P. and Coakley, J. A.: Aerosols and Climate, *Science* (1979), 183, 75–77, <https://doi.org/10.1126/science.183.4120.75>, 1974.

1420 Christensen, M. W., Carrió, G. G., Stephens, G. L., and Cotton, W. R.: Radiative impacts of free-tropospheric clouds on the properties of marine stratocumulus, *J Atmos Sci*, 70, 3102–3118, <https://doi.org/10.1175/JAS-D-12-0287.1>, 2013.

Cronk, H.: CloudSat ECMWF-AUX Auxillary Data Product Process Description and Interface Control Document, https://www.cloudsat.cira.colostate.edu/cloudsat-static/info/dl/ecmwf-aux/ECMWF-AUX.PDICD.P1_R05.rev0.pdf, 2017.

1425 D'Almeida, G. A., Koepke, P., and Shettle, E. P.: Atmospheric aerosols: global climatology and radiative characteristics, A. Deepak Pub. Hampton, Va., USA, Hampton, Va., USA SE -, <https://doi.org/10.1007/978-1-4612-0533-7> - <https://worldcat.org/title/22763033>, 1991.

Deaconu, L. T., Ferlay, N., Waquet, F., Peers, F., Thieuleux, F., and Goloub, P.: Satellite inference of water vapour and above-cloud aerosol combined effect on radiative budget and cloud-Top processes in the southeastern Atlantic Ocean, *Atmos Chem Phys*, 19, 11613–11634, <https://doi.org/10.5194/acp-19-11613-2019>, 2019.

1430 DeFlorio, M. J., Ghan, S. J., Singh, B., Miller, A. J., Cayan, D. R., Russell, L. M., and Somervill, R. C. J.: Semidirect dynamical and radiative effect of North African dust transport on lower tropospheric clouds over the subtropical North Atlantic in

CESM 1.0 Michael, Journal of Geophysical Research: Atmospheres, 119, 8284–8303, <https://doi.org/10.1038/175238c0>, 2014.

1435 Doherty, O. M. and Evan, A. T.: Identification of a new dust-stratocumulus indirect effect over the tropical North Atlantic, Geophys. Res. Lett., 41, 6935–6942, <https://doi.org/10.1002/2014GL060897>, 2014.

Eastman, R. and Wood, R.: The competing effects of stability and humidity on subtropical stratocumulus entrainment and cloud evolution from a Lagrangian perspective, J Atmos Sci, 75, 2563–2578, <https://doi.org/10.1175/JAS-D-18-0030.1>, 2018.

1440 Formenti, P. and Di Biagio, C.: Large synthesis of in situ field measurements of the size distribution of mineral dust aerosols across their life cycles, Earth Syst Sci Data, 16, 4995–5007, <https://doi.org/10.5194/essd-16-4995-2024>, 2024.

Forster, P., Storelvmo, T., Armour, K., Collins, W., Dufresne, J.-L., Frame, D., Lunt, D. J., Mauritsen, T., Palmer, M. D., Watanabe, M., Wild, M., and Zhang, H.: The Earth’s Energy Budget, Climate Feedbacks and Climate Sensitivity, in: Climate Change 2021 – The Physical Science Basis, vol. 17, edited by: Masson-Delmotte, V., Zhai, P., Pirani, A., Connors, 1445 S. L., Péan, C., Berger, S., Caud, N., Chen, Y., Goldfarb, L., Gomis, M. I., Huang, M., Leitzell, K., Lonnoy, E., Matthews, J. B. R., Maycock, T. K., Waterfield, T., Yelekçi, O., Yu, R., and Zhou, B., Cambridge University Press, 923–1054, <https://doi.org/10.1017/9781009157896.009>, 2023.

Fu, Q. and Liou, K. N.: On the Correlated k-Distribution Method for Radiative Transfer in Nonhomogeneous Atmospheres, Journal of Atmospheric Science, 49, 2139–2156, [https://doi.org/10.1175/1520-0469\(1992\)049<2139:OTCDMF>2.0.CO;2](https://doi.org/10.1175/1520-0469(1992)049<2139:OTCDMF>2.0.CO;2), 1992.

1450 Gelaro, R., McCarty, W., Suárez, M. J., Todling, R., Molod, A., Takacs, L., Randles, C. A., Darmenov, A., Bosilovich, M. G., Reichle, R., Wargan, K., Coy, L., Cullather, R., Draper, C., Akella, S., Buchard, V., Conaty, A., da Silva, A. M., Gu, W., Kim, G. K., Koster, R., Lucchesi, R., Merkova, D., Nielsen, J. E., Partyka, G., Pawson, S., Putman, W., Rienecker, M., Schubert, S. D., Sienkiewicz, M., and Zhao, B.: The modern-era retrospective analysis for research and applications, version 2 (MERRA-2), J Clim, 30, 5419–5454, <https://doi.org/10.1175/JCLI-D-16-0758.1>, 2017.

Gkikas, A., Proestakis, E., Amiridis, V., Kazadzis, S., Di Tomaso, E., Marinou, E., Hatzianastassiou, N., Kok, J. F., and García-Pando, C. P.: Quantification of the dust optical depth across spatiotemporal scales with the MIDAS global dataset (2003–2017), Atmos Chem Phys, 22, 3553–3578, <https://doi.org/10.5194/acp-22-3553-2022>, 2022.

Hahn, C. J. and Warren, S. G.: A Gridded Climatology of Clouds over Land (1971–1996) and Ocean (1954–2008) from Surface 1460 Observations Worldwide (NDP-026E)*, <https://doi.org/10.3334/CDIAC/cli.ndp026e>, 2007.

Hansen, J., Sato, M., and Ruedy, R.: Radiative forcing and climate response, Journal of Geophysical Research Atmospheres, 102, 6831–6864, <https://doi.org/10.1029/96JD03436>, 1997.

Haywood, J. M., Abel, S. J., Barrett, P., Bellouin, N., Blyth, A., Bower, K. N., Brooks, M., Carslaw, K., Coe, H., Cotterell, 1465 M., Crawford, I., Davies, N., Dingley, E., Field, P., Formenti, P., Gordon, H., de Graaf, M., Herbert, R., Johnson, B., Jones, A. C., Langridge, J., Malavelle, F., Partridge, D. G., Peers, F., Redemann, J., Stier, P., Szpek, K., Taylor, J. W., Watson-Parris, D., Wood, R., Wu, H., and Zuidema, P.: The Cloud-Aerosol-Radiation Interaction and Forcing: Year-

2017 (CLARIFY-2017) measurement campaign, *Atmos Chem Phys*, 2017, <https://doi.org/10.5194/acp-21-1049-2021>, 2020.

1470 Henderson, D. S., L'ecuyer, T., Stephens, G., Partain, P., and Sekiguchi, M.: A multisensor perspective on the radiative impacts of clouds and aerosols, *J Appl Meteorol Climatol*, 52, 853–871, <https://doi.org/10.1175/JAMC-D-12-025.1>, 2013.

Herbert, R. and Stier, P.: Satellite observations of smoke-cloud-radiation interactions over the Amazon rainforest, *Atmos Chem Phys*, 23, 4595–4616, <https://doi.org/10.5194/acp-23-4595-2023>, 2023.

1475 Herbert, R. J., Bellouin, N., Highwood, E. J., and Hill, A. A.: Diurnal cycle of the semi-direct effect from a persistent absorbing aerosol layer over marine stratocumulus in large-eddy simulations, *Atmos Chem Phys*, 20, 1317–1340, <https://doi.org/10.5194/acp-20-1317-2020>, 2020.

Hess, M., Koepke, P., and Schult, I.: Optical Properties of Aerosols and Clouds: The Software Package OPAC, *Bull Am Meteorol Soc*, 79, 831–844, [https://doi.org/10.1175/1520-0477\(1998\)079<0831:OPOAAC>2.0.CO;2](https://doi.org/10.1175/1520-0477(1998)079<0831:OPOAAC>2.0.CO;2), 1998.

1480 Huang, J., Lin, B., Minnis, P., Wang, T., Wang, X., Hu, Y., Yi, Y., and Ayers, J. K.: Satellite-based assessment of possible dust aerosols semi-direct effect on cloud water path over East Asia, *Geophys Res Lett*, 33, 2–6, <https://doi.org/10.1029/2006GL026561>, 2006.

Hunt, W. H., Winker, D. M., Vaughan, M. A., Powell, K. A., Lucker, P. L., and Weimer, C.: CALIPSO Lidar Description and Performance Assessment, *J Atmos Ocean Technol*, 26, 1214–1228, <https://doi.org/10.1175/2009JTECHA1223.1>, 2009.

1485 Jacobson, M. Z.: Effects of biomass burning on climate, accounting for heat and moisture fluxes, black and brown carbon, and cloud absorption effects, *Journal of Geophysical Research: Atmospheres*, 119, 8980–9002, <https://doi.org/10.1002/2014JD021861>, 2014.

Jethva, H., Torres, O., Waquet, F., Chand, D., and Hu, Y.: How do A-train sensors intercompare in the retrieval of above-cloud aerosol optical depth? A case study-based assessment, *Geophys Res Lett*, 41, 186–192, <https://doi.org/10.1002/2013GL058405>, 2014.

1490 Johnson, B. T., Shine, K. P., and Forster, P. M.: The semi-direct aerosol effect: Impact of absorbing aerosols on marine stratocumulus, *Quarterly Journal of the Royal Meteorological Society*, 130, 1407–1422, <https://doi.org/10.1256/qj.03.61>, 2004.

Kahn, B. H., Chahine, M. T., Stephens, G. L., Mace, G. G., Marchand, R. T., Wang, Z., Barnet, C. D., Eldering, A., Holz, R. E., Kuehn, R. E., and Vane, D. G.: Cloud type comparisons of AIRS, CloudSat, and CALIPSO cloud height and amount, *Atmos. Chem. Phys*, 1231–1248, <https://doi.org/10.5194/acp-8-1231-2008>, 2008.

1495 Kim, M. H., Omar, A. H., Tackett, J. L., Vaughan, M. A., Winker, D. M., Trepte, C. R., Hu, Y., Liu, Z., Poole, L. R., Pitts, M. C., Kar, J., and Magill, B. E.: The CALIPSO version 4 automated aerosol classification and lidar ratio selection algorithm, *Atmos Meas Tech*, 11, 6107–6135, <https://doi.org/10.5194/amt-11-6107-2018>, 2018.

1500 Kim, S. W., Berthier, S., Raut, J. C., Chazette, P., Dulac, F., and Yoon, S. C.: Validation of aerosol and cloud layer structures from the space-borne lidar CALIOP using a ground-based lidar in Seoul, Korea, *Atmos Chem Phys*, 8, 3705–3720, <https://doi.org/10.5194/acp-8-3705-2008>, 2008.

Klein, S. A., Hall, A., Norris, J. R., and Pincus, R.: Low-Cloud Feedbacks from Cloud-Controlling Factors: A Review, *Surv Geophys*, 38, 1307–1329, <https://doi.org/10.1007/s10712-017-9433-3>, 2017.

Koch, D. and Del Genio, A. D.: Black carbon semi-direct effects on cloud cover: Review and synthesis, *Atmos Chem Phys*, 10, 7685–7696, <https://doi.org/10.5194/acp-10-7685-2010>, 2010.

1505 Kok, J. F., Ridley, D. A., Zhou, Q., Miller, R. L., Zhao, C., Heald, C. L., Ward, D. S., Albani, S., and Haustein, K.: Smaller desert dust cooling effect estimated from analysis of dust size and abundance, *Nat Geosci*, 10, 274–278, <https://doi.org/10.1038/ngeo2912>, 2017.

Kok, J. F., Adebiyi, A. A., Albani, S., Balkanski, Y., Checa-Garcia, R., Chin, M., Colarco, P. R., Hamilton, D. S., Huang, Y., Ito, A., Klose, M., Li, L., Mahowald, N. M., Miller, R. L., Obiso, V., Pérez García-Pando, C., Rocha-Lima, A., and Wan, 1510 J. S.: Contribution of the world's main dust source regions to the global cycle of desert dust, *Atmos Chem Phys*, 21, 8169–8193, <https://doi.org/10.5194/acp-21-8169-2021>, 2021a.

Kok, J. F., Adebiyi, A. A., Albani, S., Balkanski, Y., Checa-Garcia, R., Chin, M., Colarco, P. R., Hamilton, D. S., Huang, Y., Ito, A., Klose, M., Leung, D. M., Li, L., Mahowald, N. M., Miller, R. L., Obiso, V., Pérez García-Pando, C., Rocha-Lima, A., Wan, J. S., and Whicker, C. A.: Improved representation of the global dust cycle using observational constraints on 1515 dust properties and abundance, *Atmos Chem Phys*, 21, 8127–8167, <https://doi.org/10.5194/acp-21-8127-2021>, 2021b.

Kok, J. F., Storelvmo, T., Karydis, V. A., Adebiyi, A. A., Mahowald, N. M., Evan, A. T., He, C., and Leung, D. M.: Mineral dust aerosol impacts on global climate and climate change, *Nat Rev Earth Environ*, 4, 71–86, <https://doi.org/10.1038/s43017-022-00379-5>, 2023.

Koren, I., Kaufman, Y. J., Remer, L. A., and Martins, J. V.: Measurement of the Effect of Amazon Smoke on Inhibition of 1520 Cloud Formation, *Science* (1979), 303, 1342–1345, <https://doi.org/10.1126/science.1089424>, 2004.

L'Ecuyer, T. S., Wood, N. B., Haladay, T., Stephens, G. L., and Stackhouse, P. W.: Impact of clouds on atmospheric heating based on the R04 CloudSat fluxes and heating rates data set, *J Geophys Res*, 113, 1–15, <https://doi.org/10.1029/2008JD00951>, 2008.

Li, J., Carlson, B. E., Yung, Y. L., Lv, D., Hansen, J., Penner, J. E., Liao, H., Ramaswamy, V., Kahn, R. A., Zhang, P., 1525 Dubovik, O., Ding, A., Lacis, A. A., Zhang, L., and Dong, Y.: Scattering and absorbing aerosols in the climate system, *Nat Rev Earth Environ*, 3, 363–379, <https://doi.org/10.1038/s43017-022-00296-7>, 2022.

Liu, Z., Vaughan, M. A., Winker, D. M., Hostetler, C. A., Poole, L. R., Hlavka, D., Hart, W., and McGill, M.: Use of probability distribution functions for discriminating between clouds and aerosol in lidar backscatter data, *Journal of Geophysical Research D: Atmospheres*, 109, 1–13, <https://doi.org/10.1029/2004JD004732>, 2004.

1530 Liu, Z., Vaughan, M., Winker, D., Kittaka, C., Getzewich, B., Kuehn, R., Omar, A., Powell, K., Trepte, C., and Hostetler, C.: The CALIPSO Lidar Cloud and Aerosol Discrimination: Version 2 Algorithm and Initial Assessment of Performance, *J Atmos Ocean Technol*, 26, 1198–1213, <https://doi.org/10.1175/2009JTECHA1229.1>, 2009.

Liu, Z., Kar, J., Zeng, S., Tackett, J., Vaughan, M., Avery, M., Pelon, J., Getzewich, B., Lee, K. P., Magill, B., Omar, A.,
1535 Lucker, P., Trepte, C., and Winker, D.: Discriminating between clouds and aerosols in the CALIOP version 4.1 data
products, *Atmos Meas Tech*, 12, 703–734, <https://doi.org/10.5194/amt-12-703-2019>, 2019.

Loeb, N. G. and Schuster, G. L.: An observational study of the relationship between cloud, aerosol and meteorology in broken
low-level cloud conditions, *Journal of Geophysical Research Atmospheres*, 113, 1–9,
<https://doi.org/10.1029/2007JD009763>, 2008.

Lu, X., Mao, F., Rosenfeld, D., Zhu, Y., Pan, Z., and Gong, W.: Satellite retrieval of cloud base height and geometric thickness
1540 of low-level cloud based on CALIPSO, *Atmos Chem Phys*, 21, 11979–12003, <https://doi.org/10.5194/acp-21-11979-2021>, 2021.

Mallet, M., Solmon, F., Nabat, P., Elguindi, N., Waquet, F., Bouniol, D., Mark Sayer, A., Meyer, K., Roehrig, R., Michou,
1545 M., Zuidema, P., Flamant, C., Redemann, J., and Formenti, P.: Direct and semi-direct radiative forcing of biomass-burning
aerosols over the southeast Atlantic (SEA) and its sensitivity to absorbing properties: a regional climate modeling study,
Atmos Chem Phys, 20, 13191–13216, <https://doi.org/10.5194/acp-20-13191-2020>, 2020.

Mamouri, R. E., Amiridis, V., Papayannis, A., Giannakaki, E., Tsaknakis, G., and Balis, D. S.: Validation of CALIPSO space-
borne-derived attenuated backscatter coefficient profiles using a ground-based lidar in Athens, Greece, *Atmos Meas Tech*,
2, 513–522, <https://doi.org/10.5194/amt-2-513-2009>, 2009.

Mauger, G. S. and Norris, J. R.: Assessing the Impact of Meteorological History on Subtropical Cloud Fraction, *J Clim*, 23,
1550 2926–2940, <https://doi.org/10.1175/2010JCLI3272.1>, 2010.

Naud, C. M., Elsaesser, G. S., and Booth, J. F.: Dominant Cloud Controlling Factors for Low-Level Cloud Fraction:
Subtropical Versus Extratropical Oceans, *Geophys Res Lett*, 50, 1–10, <https://doi.org/10.1029/2023GL104496>, 2023.

Nayak, M., Witkowski, M., Vane, D., Livermore, T., Rokey, M., Barthuli, M., Gravseth, I. J., Pieper, B., Rodzinak, A., Silva,
1555 S., and Woznick, P.: CloudSat Anomaly Recovery and Operational Lessons Learned, in: SpaceOps 2012 Conference,
<https://doi.org/10.2514/6.2012-1295798>, 2012.

Omar, A. H., Winker, D. M., Kittaka, C., Vaughan, M. A., Liu, Z., Hu, Y., Trepte, C. R., Rogers, R. R., Ferrare, R. A., Lee,
K. P., Kuehn, R. E., and Hostetler, C. A.: The CALIPSO automated aerosol classification and lidar ratio selection
algorithm, *J Atmos Ocean Technol*, 26, 1994–2014, <https://doi.org/10.1175/2009JTECHA1231.1>, 2009.

Perrone, M. R., De Tomasi, F., and Burlizzi, P.: Aerosol products by CALIOP at 532 nm and by a ground-based Raman lidar
1560 at 355 nm: Intercomparison methodology, *Atmos Res*, 101, 438–449, <https://doi.org/10.1016/j.atmosres.2011.04.005>,
2011.

Prospero, J. M., Delany, A. C., Delany, A. C., and Carlson, T. N.: The discovery of african dust transport to the western
hemisphere and the Saharan air layer: A history, *Bull Am Meteorol Soc*, 102, E1239–E1260,
<https://doi.org/10.1175/BAMS-D-19-0309.1>, 2021.

1565 Rajapakshe, C., Zhang, Z., Yorks, J. E., Yu, H., Tan, Q., Meyer, K., Platnick, S., and Winker, D. M.: Seasonally transported aerosol layers over southeast Atlantic are closer to underlying clouds than previously reported, *Geophys Res Lett*, 44, 5818–5825, <https://doi.org/10.1002/2017GL073559>, 2017.

1570 Ricchiazzi, P., Yang, S., Gautier, C., and Sowle, D.: SBDART: A Research and Teaching Software Tool for Plane-Parallel Radiative Transfer in the Earth's Atmosphere, *Bull Am Meteorol Soc*, 79, 2101–2114, [https://doi.org/10.1175/1520-0477\(1998\)079<2101:SARATS>2.0.CO;2](https://doi.org/10.1175/1520-0477(1998)079<2101:SARATS>2.0.CO;2), 1998.

Ryder, C. L.: Radiative Effects of Increased Water Vapor in the Upper Saharan Air Layer Associated With Enhanced Dustiness, *Journal of Geophysical Research: Atmospheres*, 126, <https://doi.org/10.1029/2021JD034696>, 2021.

1575 Ryder, C. L., Highwood, E. J., Rosenberg, P. D., Trembath, J., Brooke, J. K., Bart, M., Dean, A., Crosier, J., Dorsey, J., Brindley, H., Banks, J., Marsham, J. H., McQuaid, J. B., Sodemann, H., and Washington, R.: Optical properties of Saharan dust aerosol and contribution from the coarse mode as measured during the Fennec 2011 aircraft campaign, *Atmos Chem Phys*, 13, 303–325, <https://doi.org/10.5194/acp-13-303-2013>, 2013.

1580 Ryder, C. L., Marenco, F., Brooke, J. K., Estelles, V., Cotton, R., Formenti, P., McQuaid, J. B., Price, H. C., Liu, D., Ausset, P., Rosenberg, P. D., Taylor, J. W., Choularton, T., Bower, K., Coe, H., Gallagher, M., Crosier, J., Lloyd, G., Highwood, E. J., and Murray, B. J.: Coarse-mode mineral dust size distributions, composition and optical properties from AER-D aircraft measurements over the tropical eastern Atlantic, *Atmos Chem Phys*, 18, 17225–17257, <https://doi.org/10.5194/acp-18-17225-2018>, 2018.

Ryder, C. L., Highwood, E. J., Walser, A., Seibert, P., Philipp, A., and Weinzierl, B.: Coarse and giant particles are ubiquitous in Saharan dust export regions and are radiatively significant over the Sahara, *Atmos Chem Phys*, 19, 15353–15376, <https://doi.org/10.5194/acp-19-15353-2019>, 2019.

1585 Sakai, T., Nagai, T., Zaizen, Y., and Mano, Y.: Backscattering linear depolarization ratio measurements of mineral, sea-salt, and ammonium sulfate particles simulated in a laboratory chamber, *Appl Opt*, 49, 4441–4449, <https://doi.org/10.1364/AO.49.004441>, 2010.

1590 Sand, M., Samset, B. H., Myhre, G., Gliß, J., Bauer, S. E., Bian, H., Chin, M., Checa-Garcia, R., Ginoux, P., Kipling, Z., Kirkevåg, A., Kokkola, H., Le Sager, P., Lund, M. T., Matsui, H., Van Noije, T., Olivié, D. J. L., Remy, S., Schulz, M., Stier, P., Stjern, C. W., Takemura, T., Tsigaridis, K., Tsyro, S. G., and Watson-Parris, D.: Aerosol absorption in global models from AeroCom phase III, *Atmos Chem Phys*, 21, 15929–15947, <https://doi.org/10.5194/acp-21-15929-2021>, 2021.

Sandu, I. and Stevens, B.: On the Factors Modulating the Stratocumulus to Cumulus Transitions, *J Atmos Sci*, 68, 1865–1881, <https://doi.org/10.1175/2011JAS3614.1>, 2011.

1595 Satheesh, S. and Krishnamoorthy, K.: Radiative effects of natural aerosols: A review, *Atmos Environ*, 39, 2089–2110, <https://doi.org/10.1016/j.atmosenv.2004.12.029>, 2005.

Schneider, D. P., Deser, C., Fasullo, J., and Trenberth, K. E.: Climate Data Guide Spurs Discovery and Understanding, *Eos, Transactions American Geophysical Union*, 94, 121–122, <https://doi.org/10.1002/2013EO130001>, 2013.

Scott, R. C., Myers, T. A., Norris, J. R., Zelinka, M. D., Klein, S. A., Sun, M., and Doelling, D. R.: Observed sensitivity of
1600 low-cloud radiative effects to meteorological perturbations over the global oceans, *J Clim*, 33, 7717–7734,
<https://doi.org/10.1175/JCLI-D-19-1028.1>, 2020.

Singer, C. E. and Schneider, T.: CO₂-driven stratocumulus cloud breakup in a bulk boundary layer model,
<https://doi.org/10.22541/essoar.168167204.45220772/v1>, 2023.

Stubenrauch, C. J., Rossow, W. B., Kinne, S., Ackerman, S., Cesana, G., Chepfer, H., Di Girolamo, L., Getzewich, B.,
1605 Guignard, A., Heidinger, A., Maddux, B. C., Menzel, W. P., Minnis, P., Pearl, C., Platnick, S., Poulsen, C., Riedi, J., Sun-
Mack, S., Walther, A., Winker, D., Zeng, S., and Zhao, G.: Assessment of global cloud datasets from satellites: Project
and database initiated by the GEWEX radiation panel, *Bull Am Meteorol Soc*, 94, 1031–1049,
<https://doi.org/10.1175/BAMS-D-12-00117.1>, 2013.

Tackett, J. L., Winker, D. M., Getzewich, B. J., Vaughan, M. A., Young, S. A., and Kar, J.: CALIPSO lidar level 3 aerosol
1610 profile product: version 3 algorithm design, *Atmos Meas Tech*, 11, 4129–4152, <https://doi.org/10.5194/amt-11-4129-2018>, 2018.

Twomey, S.: Pollution and the Planetary Albedo, *Atmos Environ*, 8, 1251–1256,
<https://doi.org/10.1016/j.atmosenv.2007.10.062>, 1974.

Vaughan, M. A., Winker, D. M., and Hostetler, C. A.: SIBYL: a selective iterated boundary location algorithm for finding
1615 cloud and aerosol layers in CALIPSO lidar data, *Lidar Remote Sensing in Atmospheric and Earth Sciences*, 791–794,
2002.

Vaughan, M. A., Powell, K. A., Kuehn, R. E., Young, S. A., Winker, D. M., Hostetler, C. A., Hunt, W. H., Liu, Z., McGill, M.
J., and Getzewich, B. J.: Fully automated detection of cloud and aerosol layers in the CALIPSO lidar measurements, *J Atmos Ocean Technol*, 26, 2034–2050, <https://doi.org/10.1175/2009JTECHA1228.1>, 2009.

1620 Volz, F. E.: Infrared Refractive Index of Atmospheric Aerosol Substances, *Appl Opt*, 11, 755,
<https://doi.org/10.1364/ao.11.000755>, 1972.

Weinzierl, B., Ansmann, A., Prospero, J. M., Althausen, D., Benker, N., Chouza, F., Dollner, M., Farrell, D., Fomba, W. K.,
Freudenthaler, V., Gasteiger, J., Groß, S., Haarig, M., Heinold, B., Kandler, K., Kristensen, T. B., Mayol-Bracero, O. L.,
Müller, T., Reitebuch, O., Sauer, D., Schäfler, A., Schepanski, K., Spanu, A., Tegen, I., Toledano, C., and Walser, A.:
1625 The Saharan aerosol long-range transport and aerosol-cloud-interaction experiment: Overview and selected highlights,
Bull Am Meteorol Soc, 98, 1427–1451, <https://doi.org/10.1175/BAMS-D-15-00142.1>, 2017.

Wilcox, E. M.: Stratocumulus cloud thickening beneath layers of absorbing smoke aerosol, *Atmos Chem Phys*, 10, 11769–
11777, <https://doi.org/10.5194/acp-10-11769-2010>, 2010.

Wilcox, E. M.: Direct and semi-direct radiative forcing of smoke aerosols over clouds, *Atmos Chem Phys*, 12, 139–149,
1630 <https://doi.org/10.5194/acp-12-139-2012>, 2012.

Wilcox, E. M., Harshvardhan, and Platnick, S.: Estimate of the impact of absorbing aerosol over cloud on the MODIS retrievals of cloud optical thickness and effective radius using two independent retrievals of liquid water path, *Journal of Geophysical Research Atmospheres*, 114, 1–7, <https://doi.org/10.1029/2008JD010589>, 2009.

Winker, D. M., Pelon, J., CoakleyJr, J. A., Ackerman, S. A., Charlson, R. J., Colarco, P. R., Flamant, P., Fu, Q., Hoff, R. M.,
1635 Kittaka, C., Kubar, T. I., Treut, H. Le, McCormick, M. P., Mégie, G., Poole, L., Powell, K., Trepte, C., Vaughan, M. A., and Wielick, B. A.: The CALIPSO Mission, *Bulletin of American Meteorological Society*, 91, 1211–1230, <https://doi.org/10.1175/2010bams3009.1>, 2010.

Wiscombe, W. J.: Improved Mie scattering algorithms, *Appl Opt*, 19, 1505, <https://doi.org/10.1364/ao.19.001505>, 1980.

Witkowski, M. M., Vane, D., and Livermore, T.: CloudSat - Life in Daylight Only Operations (DO-Op), in: 2018 SpaceOps
1640 Conference, 1–14, <https://doi.org/10.2514/6.2018-2562>, 2018.

Wood, R.: Stratocumulus clouds, *Mon Weather Rev*, 140, 2373–2423, <https://doi.org/10.1175/MWR-D-11-00121.1>, 2012.

Wood, R. and Bretherton, C. S.: On the relationship between stratiform low cloud cover and lower-tropospheric stability, *J Clim*, 19, 6425–6432, <https://doi.org/10.1175/JCLI3988.1>, 2006.

Yamaguchi, T., Feingold, G., Kazil, J., and McComiskey, A.: Stratocumulus to cumulus transition in the presence of elevated
1645 smoke layers, *Geophys Res Lett*, 42, 10478–10485, <https://doi.org/10.1002/2015GL066544>, 2015.

Yu, H., Chin, M., Bian, H., Yuan, T., Prospero, J. M., Omar, A. H., Remer, L. A., Winker, D. M., Yang, Y., Zhang, Y., and
Zhang, Z.: Quantification of trans-Atlantic dust transport from seven-year (2007–2013) record of CALIPSO lidar
measurements, *Remote Sens Environ*, 159, 232–249, <https://doi.org/10.1016/j.rse.2014.12.010>, 2015.

Zheng, J., Zhang, Z., Yu, H., Garnier, A., Song, Q., Wang, C., Di Biagio, C., Kok, J. F., Derimian, Y., and Ryder, C.: Thermal
1650 infrared dust optical depth and coarse-mode effective diameter over oceans retrieved from collocated MODIS and
CALIOP observations, *Atmos Chem Phys*, 23, 8271–8304, <https://doi.org/10.5194/acp-23-8271-2023>, 2023.

Zuidema, P., Redemann, J., Haywood, J., Wood, R., Piketh, S., Hipondoka, M., and Formenti, P.: Smoke and clouds above
the southeast Atlantic: Upcoming field campaigns probe absorbing aerosol's impact on climate, *Bull Am Meteorol Soc*,
97, 1131–1135, <https://doi.org/10.1175/BAMS-D-15-00082.1>, 2016.

1655 Zuidema, P., Alvarez, C., Kramer, S. J., Custals, L., Izaguirre, M., Sealy, P., Prospero, J. M., and Blades, E.: Is summer African
dust arriving earlier to Barbados? The updated long-term in-situ dust mass concentration time series from Ragged Point,
Barbados and Miami, Florida, *Bull Am Meteorol Soc*, 1981–1986, <https://doi.org/10.1175/bams-d-18-0083.1>, 2019.